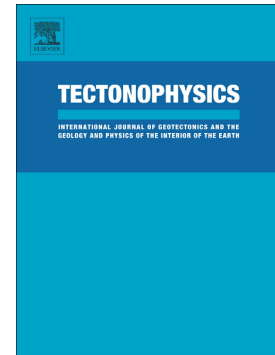


Accepted Manuscript

Persistent rupture terminations at a restraining bend from slip rates on the eastern Altyn Tagh Fault

A.J. Elliott, M.E. Oskin, J. Liu-zeng, Y.-X. Shao



PII: S0040-1951(18)30004-0
DOI: <https://doi.org/10.1016/j.tecto.2018.01.004>
Reference: TECTO 127742
To appear in: *Tectonophysics*
Received date: 31 July 2017
Revised date: 22 December 2017
Accepted date: 3 January 2018

Please cite this article as: A.J. Elliott, M.E. Oskin, J. Liu-zeng, Y.-X. Shao , Persistent rupture terminations at a restraining bend from slip rates on the eastern Altyn Tagh Fault. The address for the corresponding author was captured as affiliation for all authors. Please check if appropriate. Tecto(2017), <https://doi.org/10.1016/j.tecto.2018.01.004>

This is a PDF file of an unedited manuscript that has been accepted for publication. As a service to our customers we are providing this early version of the manuscript. The manuscript will undergo copyediting, typesetting, and review of the resulting proof before it is published in its final form. Please note that during the production process errors may be discovered which could affect the content, and all legal disclaimers that apply to the journal pertain.

Persistent Rupture Terminations at a Restraining Bend from Slip Rates on the eastern Altyn Tagh Fault

A. J. Elliott^{1*}, M. E. Oskin², J. Liu-zeng³, Y.-X. Shao^{3,4}

1 - University of Oxford Department of Earth Sciences

2 - University of California Davis Department of Earth and Planetary Sciences

3 - State Key Laboratory of Earthquake Dynamics, Institute of Geology, China Earthquake Administration

4 - Lanzhou Institute of Seismology, China Earthquake Administration

Abstract

Restraining double-bends along strike-slip faults inhibit or permit throughgoing ruptures depending on bend angle, length, and prior rupture history. Modeling predicts that for mature strike-slip faults in a regional stress regime characterized by simple shear, a restraining bend of $>18^\circ$ and >4 km length impedes propagating rupture. Indeed, natural evidence shows that the most recent rupture(s) of the Xorkoli section (90° – 93° E) of the eastern Altyn Tagh Fault (ATF) ended at large restraining bends. However, when multiple seismic cycles are considered in numerical dynamic rupture modeling, heterogeneous residual stresses enable some ruptures to propagate further, modulating whether the bends persistently serve as barriers. These models remain to be tested using observations of the cumulative effects of multiple earthquake ruptures. Here we investigate whether a large restraining double-bend on the ATF serves consistently as a barrier to rupture by measuring long-term slip rates around the terminus of its most recent surface rupture at the Aksay bend. Our results show a W—E decline in slip as the SATF enters the bend, as would be predicted from repeated rupture terminations there. Prior work demonstrated no Holocene slip on the central, most misoriented portion of the bend, while 19 – 79 m offsets suggest that multiple ruptures have occurred on the west side of the bend during the Holocene. Thus we conclude the gradient in the SATF's slip rate results from the repeated termination of earthquake ruptures there. However, a finite slip rate east of the bend represents the transmission of some slip, suggesting that a small fraction of ruptures may fully traverse or jump the double-bend. This agreement between natural observations of slip accumulation and multi-cycle models of fault rupture enables us to translate observed slip rates into insight about the dynamic rupture process of individual earthquakes as they encounter geometric complexities along faults.

*Corresponding author: ajelliott@ucdavis.edu; South Parks Road, Oxford, UK OX1 3AN

1 Introduction

Bends and stepovers in strike-slip faults introduce stress heterogeneities that impact seismic rupture propagation, potentially limiting the length of a fault rupture and the magnitude of the resulting earthquake (*King and Nábělek, 1985; Harris and Day, 1993; Duan and Oglesby, 2005, 2006; Lozos et al., 2011*). Model results and natural observations have shown that discontinuous stepovers >4 km wide impede rupture propagation (*Harris and Day, 1993; Duan and Oglesby, 2006; Wesnousky, 2006*), but an unresolved question is whether linked stepovers—fault double-bends—produce similarly systematic behavior in nature, as predicted by numerical models.

Numerical simulations of individual fault ruptures at double-bends of different angles underscore the primary control bend angle has in modulating whether ruptures pass through or terminate at fault bends (*Lozos et al., 2011*). The simulations of *Lozos et al. (2011)* indicate that in the absence of a heterogeneous stress field from prior events, fault bends of $>18^\circ$ reliably halt propagating ruptures. However, when multiple seismic cycles are considered, ruptures may propagate further thanks to high residual stresses left at the ends of prior ruptures. Through numerical simulations of dynamic rupture at a simple fault bend, *Duan and Oglesby (2005)* find quasi-periodic recurrence of rupture termination location due to a combination of static fault geometry and the evolving stress field left by successive ruptures (Fig. 1).

Slip accumulates across stepover and bend structures over multiple earthquake cycles in a distribution that reflects fault zone mechanics as well as dynamic seismic behavior, permitting us to compare geologic observations with numerical rupture-modelling results to characterize seismic behavior at these geometric complexities. The quasi-periodic repetition of rupture extents in the modeling of *Duan and Oglesby (2005)* produces a systematic gradient in accumulated slip, as well as differences along strike in the number of events over time (Fig. 1)—observables that we can test in nature.

Here we investigate accumulated slip along a major transpressional double-bend in the left-lateral Altyn Tagh Fault in order to test how its substantial change in strike (25°) exerts a control on earthquake rupture extents. Because of its exceptionally linear geometry, punctuated by major restraining bends, the Altyn Tagh fault can provide insight into the impact of geometric complexities on fault slip rate and seismogenesis. At the Aksay bend of the sinistral Altyn Tagh Fault in western Gansu Province, China (92.5°E – 94.5°E) *Elliott et al. (2015)* and *Washburn et al. (2001)* have documented the terminations of a historic rupture (or two) at the fault's large

restraining bends. We seek to understand whether this behavior persists through multiple earthquake cycles. *Washburn et al.* (2001) identified two or three surface-rupturing events where this most recent one occurred to the west of the bend, none of which appear to have ruptured through the bend according to undeformed geomorphic features within the bend documented by *Elliott et al.* (2015). Here we present four new slip rates at different positions along the bend, showing an abrupt west to east decrease in slip rate as the fault bends, and a further decrease to less than 20% of these values on the other, eastern side of the bend. Our observations corroborate the predictions of numerical modeling by *Duan and Oglesby* (2005) and *Lozos et al.* (2011), indicating both that high bend angle limits the ability of fault rupture to propagate through a linked stepover, but also that this behavior may occasionally be overridden. The correspondence of these observations with model results based on rupture physics leads us to conclude that there are rare bend-breaching ruptures enabled by residual stresses built up after a series of large earthquakes have halted within the bend.

2 Predictions of Restraining Bend Behavior from Numerical Models

Relatively high Coulomb failure stresses arise within a bend in a strike-slip fault because of the increased ratio of normal to shear stress resolved onto a fault segment oriented at a higher angle to the principal stress direction in a regional stress field. Thus, fault restraining bends are hypothesized to impede propagating rupture, potentially stifling an earthquake altogether (e.g., *King and Nábělek*, 1985). Physics-based modeling of rupture at fault bends exhibits this phenomenon, but specific rupture behaviors, including amount of slip, velocity, and length, vary depending on both static and evolving stresses within the modeled system (*Duan and Oglesby*, 2005; *Lozos et al.*, 2011).

Multi-cycle modeling of spontaneous earthquake ruptures by *Duan and Oglesby* (2005) suggests that stress heterogeneities due to fault bends may produce quasi-regular groups of earthquakes that terminate at predictable locations. They model elastodynamic rupture along a simple 40-km-long fault system with a 20° restraining bend embedded in a 2D elastic medium, incorporating a viscoelastic interseismic period to account for off-fault deformation and tectonic loading. After many seismic cycles the stress field and rupture recurrence stabilize into a roughly repeating pattern of four distinct event types, which illuminate the role of evolving residual stresses in modulating behavior induced by geometry alone (Fig. 1). Their first event ruptures

only the favorable portion of the fault; a second event additionally ruptures part-way into the unfavorable section, enabled by heightened residual stress at the tip of the first rupture. After that residual stress is relieved by the second event, the third event is once again impeded by the unfavorable section. Finally, a fourth event ruptures the full length of the fault thanks to sufficient residual stresses to sustain it past the tip of each prior rupture (Fig. 1). These simulations of dynamic rupture at a fault bend reveal both a distinctive gradient in cumulative slip and a difference in the number of events at a given position along the fault (Fig. 1). The model results provide observable metrics that may be investigated in the field to probe the behavior of a natural fault system. We would expect paleoseismology to show a decreasing number of events with increasing distance into the bend. Furthermore, the models predict a spatial decline toward the bend of accumulated slip after multiple earthquake cycles.

3 Setting & Active Tectonics of the Altyn Tagh Fault

3.1 Geologic setting of ATF

The Altyn Tagh fault forms a major lithospheric boundary between the Tibet-Qinghai Plateau to the south and the Tarim Basin to the north (Fig. 2c). This 1800-km-long left-lateral strike-slip fault forms a structural, geological, and topographic boundary on the northwestern margin of the plateau, accommodating relative eastward motion of the plateau relative to stable Eurasia (*Molnar and Tapponnier, 1975; Peltzer et al., 1989; Tapponnier et al., 1990; Houseman and England, 1993; Avouac and Tapponnier, 1993; England and Molnar, 1997a, 1997b, 2005*). The fault is among the largest strike-slip faults in the world, with ~450 km of accumulated offset along its length between 82°E and 95°E (*Ritts and Biffi, 2000; Yin and Harrison, 2000; Yue et al., 2001; Cowgill et al., 2003*). Its surface trace is continuous and remarkably straight, except where it is punctuated by four large restraining double-bends. The easternmost of these double-bends is located near the town of Aksay at ~93.6°E (Fig. 2a, e.g., *Tapponnier and Molnar, 1977; Cowgill et al., 2004*). At this reach of the fault two strands overlap for ~200 km, where both take a 25 km rightward step through a restraining double-bend (Fig. 2b, *Tapponnier and Molnar, 1977; Delville et al., 2001; Wang et al., 2004; Mériaux et al., 2005*).

3.2 Geometry of the Aksay bend

Over the course of the Aksay bend, the ATF system comprises two subparallel but disconnected strands, 5 to 17 km apart, with the southern strand (SATF) continuing westward and the northern strand (NATF) continuing eastward (Fig. 2a). Although the faults overlap each other in a releasing sense, (i.e., left-stepping on a left-lateral fault), both exhibit a 25 km *rightward* step, amounting to a net ~ 15 km rightward, *restraining* step in the dominant active trace of the left-lateral ATF (Fig. 2). Across the Aksay double-bend, principal strike-slip deformation is transferred from one to the other of its paired strands. This kinematic situation enables investigation of the bend's effect on earthquake ruptures incoming from either direction (Fig. 2b). Along single-stranded fault double-bends, the extents of prehistoric earthquake ruptures can be difficult or impossible to distinguish where they may overlap or approach one another within the bends, and where fault slip rate is conserved from one side of the bend to the other. In contrast, at the Aksay bend the transfer of slip between overlapping faults permits tracking of cumulative slip from ruptures that end within the bend without an overprinted signal of large incoming earthquakes from the other side.

With this configuration, slip rates along the SATF only represent a fraction of the full slip rate across this tectonic boundary. Importantly, the northern strand does not exhibit the same evidence for recent surface rupture as the SATF at this longitude (*Elliott et al.*, 2015). Furthermore, the Annanba Valley Fault (AVF on Figs. 2b, 3, & Supplemental Figure S2), which branches northward from the SATF toward the NATF, does not exhibit surface rupture from this same most recent SATF event. In fact, as described further in §5.5 and the Supplementary Material, the AVF exhibits neither direct connectivity with the NATF nor as high a slip rate as the SATF beyond their branching point, indicating that it is a relatively uncommonly ruptured portion of the system and revealing the lack of regular seismic connectivity between the SATF and NATF.

3.3 Prior Slip Rates on the Altyn Tagh Fault

Geologic slip rates across the ATF near Aksay bend have been calculated over a range of timescales, with estimates of Late Quaternary rates ranging from 7 to 27 mm yr⁻¹ (*Tapponnier et al.*, 2001; *van der Woerd et al.*, 2001; *Wang et al.*, 2004; *Mériaux et al.*, 2005; *Xu et al.*, 2005; *Zhang et al.*, 2007; *Chen et al.*, 2013). Estimates at the upper end of this range (e.g., *Mériaux*

et al., 2005; *Xu et al.*, 2005) have been disputed by subsequent studies on the basis of alternative geomorphic interpretations, and the most recent estimates range more tightly between 7 and 12 mm yr⁻¹ (*Zhang et al.*, 2007; *Chen et al.*, 2013). Slip rates measured geodetically across this fault zone, encompassing both the NATF and SATF strands, tend between 8 and 11 mm yr⁻¹ (*Bendick et al.*, 2000; *Gan et al.*, 2007; *Thatcher*, 2007; *Zhang et al.*, 2007; *Jolivet et al.*, 2008), and more recent geologic investigations farther west have found general agreement with these rates (*Zhang et al.*, 2007; *Cowgill et al.*, 2009; *Gold et al.*, 2011).

3.4 Earthquake History on the Altyn Tagh Fault

While a 25 km-long western reach of the Altyn Tagh Fault ruptured in a M_w6.9 earthquake in 2015 (*Li et al.*, 2016), there are no historical records of rupture along the eastern portion. Nonetheless, many workers have reported morphologic evidence of surface rupture along the central and eastern ATF that appears no more than a few centuries old (*Molnar et al.*, 1987; *Washburn et al.*, 2001; *Wang et al.*, 2002; *Washburn and Arrowsmith*, 2003; *Mériaux et al.*, 2005; *Elliott et al.*, 2015). *Washburn et al.* (2001) and *Elliott et al.* (2015) report detailed surface traces and slip distributions along the central reach of the fault between the Akato Tagh and Aksay bends (Fig. 2). *Gao et al.* (2017) document 7 m offsets on the NATF east of Aksay bend, which may represent a single event offset, but report the absence of fresh morphology and numerous offsets that would suggest a recent surface break. *Elliott et al.* (2015) identify the well defined eastward termination of surface rupture in the most recent event on the SATF, which coincides with the portion of the fault within Aksay bend most highly misoriented from regional strike and thus least geometrically favorable for rupture.

Paleoseismologic investigations along this recently ruptured reach of the SATF to the west of Aksay bend reveal two or three additional events in the past 2.2–3.0 kyr, with recurrence intervals of either ~700 to 1100 years (*Washburn et al.*, 2001; *Washburn et al.*, 2003). Meanwhile *Elliott et al.* (2015) reports that no earthquakes have ruptured the most unfavorably oriented portion of the fault in the Holocene. Together these pieces of evidence strongly suggest that most, if not all, ruptures of the SATF terminate at the bend.

However, paleoseismology only coarsely defines rupture extents, and geomorphology alone rarely provides a record of rupture extents beyond the single most recent earthquake along a given reach of fault, so we must rely on the corroboration of longer term slip records with

physics-based modeling to understand the variability in rupture behavior. To assess this behavior, we present four new geologic slip rate measurements from the SATF as its activity declines through at Aksay bend, from the Xinjiang-Gansu border ($\sim 92.95^\circ\text{E}$) to east of the double-bend at Dangjin Pass ($\sim 94.42^\circ\text{E}$, Fig. 2).

4 Methods

4.1 Strike-slip from fluvial risers and incised channels

We calculate strike-slip displacement rates by measuring the magnitudes of sinistral offsets and the associated abandonment ages of landforms that have been cut by the fault. Measuring lateral slip rates requires approximately linear, ideally fault-orthogonal features that form piercing lines. Specifically, we measure offsets recorded by narrow incised channels in alluvial fan deposits, and steep inter-terrace risers that separate fluvial terrace levels of different ages. Both incised channels and terrace risers result from abandonment of and incision into the surfaces of existing deposits, although incision may initiate locally long after surface abandonment. Thus the abandonment age of an incised surface gives the maximum age of the channels that have incised it. However, where an incised channel represents the course of the main channel, its incision necessarily coincides with abandonment of the surface it is inset into, as the catchment has no other possible outlet. The abandonment age of an upper surface may not, however, be the best constraint on the age of a riser between two fluvial terraces, because riser refreshment may occur during occupation of the lower terrace level, re-forming the riser until abandonment of the *lower* terrace. For a full treatment of the upper/lower terrace age ambiguity and strategies to address it, consult *Zhang et al. (2007)*, *Cowgill et al. (2009)*, and *Gold et al. (2009)*. Our investigations here address the ambiguity in riser age by measuring offsets of primary microtopographic depositional features on offset surfaces rather than relying on fluvial risers alone (e.g., see Ta Si He site below), and by evaluating cross-cutting relationships that define the relative ages of geomorphic features (e.g., see Dangjin Shankou site below).

Geochronologic dates are reported with $2\text{-}\sigma$ analytical uncertainty. When combining offset and age to obtain slip rate, uncertainties are defined conservatively by incorporating minimum and maximum permissible values based on the uncertainty bounds of both offset and age (i.e.,

minimum offset and maximum age give minimum slip rate; maximum offset and minimum age give maximum slip rate).

4.2 Topographic surveys

Offsets were measured in the field using a survey tape aligned along the fault between up- and downstream projections of offset piercing lines. These measurements were supplemented, or where impossible to make, replaced, by topographic surveys with either Total Station or differential GPS. We conducted surveys using a Leica Total Station and pole-mounted reflective prism. Range and azimuth measurements from the Total Station have a stated precision of 2 mm and 2 arc seconds, respectively; positioning and leveling of the prism rod represent the greatest source of error in Total Station surveys, amounting to ≤ 10 cm of horizontal positioning uncertainty and ≤ 2 cm vertical. Differential GPS surveys were conducted with two Trimble GeoExplorer 3000 handheld GPS units. Concurrent logging of a stationary base station with one of the devices permits correction of the data from the roving unit for orbital and atmospheric artifacts. Horizontal accuracy of point positions after differential correction reported in Trimble Pathfinder office is < 15 cm for $> 75\%$ of the points. These surveys both permit quantification of fault offsets and aid in mapping and interpretation of geomorphic landforms.

4.3 OSL Geochronology

Accumulating tectonic offsets are preserved only after stabilization of a landform. Thus, the maximum ages of measured offsets are represented by the abandonment age of the associated landform. Along the Altyn Tagh Fault where it forms the eastern boundary of the Tarim Basin, the linear mountain ranges represent the first barrier to prevailing winds off of the Taklimakan Desert (*Sun, 2002a, 2002b*). Aeolian loess accumulates atop surfaces on the west flanks of these ranges during regional dust storms where high topography blocks surface winds and silt settles out (e.g., *Lehmkuhl et al., 2000; Sun et al., 2007*). The loess forms thick capping deposits that are only preserved where water no longer regularly flows. The onset of loess accumulation thus marks the abandonment of a surface by regular fluvial or alluvial flows, as this fine material is easily reworked and removed by flowing water. Thus the burial age of the basal layers of a surface-capping loess deposit provide a minimum abandonment age of that geomorphic surface. Abundant loess deposits capping all geomorphic surfaces throughout the Aksay region provide

ample material for optically stimulated luminescence (OSL) burial-age dating of fine quartz grains. This common Quaternary geochronometer relies on burial of material from exposure to visible radiation, i.e., sunlight (*Rhodes, 2011*), and has been used effectively throughout this arid region of interior Asia (*Lehmkuhl et al., 2000; Pan et al., 2003; Porter and An, 2005; Owen et al., 2006; Sun et al., 2007; Chen et al., 2012, 2013*). Sample collection, processing, and considerations are described in the Supplementary Material.

Where suitable material was present, we supplemented our OSL measurements with radiocarbon dates or Beryllium-10 exposure ages to independently verify the geochronology. The OSL results are reported in Table 1, and the C-14 data are reported in Table 2.

5 New Slip Rates at the Aksay Bend

Here we report calculated slip rates for four sites on the SATF to characterize fault zone slip rates on either side of the Aksay double-bend. Below we describe the geomorphology of each site, explain the geochronologic measurements, and then discuss the interpretation of slip rate derived at each site.

5.1 92.95°E Xinjiang Border Site

In the southwest corner of Annanba Valley, ~2 km east of the Xinjiang-Gansu border, at 92.952°E 39.212°N, the SATF cuts and offsets an incised alluvial bajada. The drainages incised into this bajada are offset a uniform amount across the fault, allowing robust reconstruction of the magnitude of slip since abandonment of the alluvial surface and establishment of the incised channel network (Fig. 4).

The westernmost modern basin deposit in the Annanba Valley is a narrow alluvial fan complex just east of the Xinjiang-Gansu border. Here alluvial fans fed by small catchments coalesce into a narrow bajada (Fig. 4). The bajada comprises two main abandoned alluvial fan surfaces, distinguished by substantial differences in height above the modern channel and in depth of loess cover. The fans are formed where north-flowing drainages open into Annanba Valley across the SATF, and extend ~100–200 m across this narrow end of the valley to their convergence with a transverse river, which flows eastward to its junction with the main Annanba River (Fig. 4). The fan deposits are composed of <20 cm subangular, locally sourced gneissic clasts, as well as larger (10–50 cm) rounded clasts recycled from older fan deposits now being

incised on the other side of the fault. The fans are deeply covered in loess. The lower surface (Q1) is overlain by loess with a depth of ~ 50 cm. The loess deposit on the higher surface (Q2) varies substantially in depth, from 80 to >200 cm, possibly due to loess infilling of original bar-and-swale topography. A 4 m tall riser separates Q1 and Q2; this riser along with the greater depth of loess accumulation on Q2 indicate that the surface is of greater age than Q1.

Incised into the Q2 surface are ten 2- to 5-m-deep channels, labeled alphabetically A-J from west to east in Figure 4. The same number of channels exist up- and down-stream of the fault along the reach of this bajada. The thalwegs of these channels were surveyed with differential GPS. Channel width can be directly measured from Quickbird imagery and is roughly proportional to channel depth. Each of these channels exhibits a left deflection across the fault, with upstream connectivity generally maintained through the lengthening of each channel along the fault (Fig. 4). Reconstruction of these deflections by 54 ± 5 m into alignment across the fault results in a poor match of upstream and downstream channel cross-sectional areas (Supplemental Fig. S2), suggesting that total displacement of each feature is higher than that represented by the deflections of the continuous modern channels. Additional right-lateral backslip totaling 79 ± 5 m aligns channels with matching up- and downstream cross-sectional areas (Fig. 4b), and we thus interpret this value to represent the accumulated fault slip since formation of these channels at the fault.

We excavated a 100-cm-deep pit into the Q2 surface to sample the basal loess for OSL burial age dating. The gravel Q2 deposit is directly overlain by 20 cm of finely laminated silt, which is in turn overlain by 60 cm of massive fine silt. The lower unit is composed predominantly of subangular, silt-sized quartz grains, with a distribution of clast sizes and composition much more similar to the massive fine silt deposit above than the gravel deposit below. We collected OSL samples from both of these layers (one 5 cm above the gravel and one 25 cm above the gravel). Laboratory analysis indicates a date of 19.1 ± 1 ka for the lower sample. The sample collected from 55 cm depth at the base of the massive loess returns a date of 16.4 ± 0.5 ka.

Incision of the channels into the older alluvial fan surface must coincide with abandonment of the Q2 fan surface, as the channels represent the unique courses of upstream drainages. The lowering of base level that drove this incision could have been climatic, or alternatively tectonically driven by decreases in downstream elevation due to incremental juxtaposition of relatively lower parts of Annanba Valley. Alternatively the incision may have been driven by

southward migration of the transverse river. In any case, the incision event marks abandonment of Q2 and thus is dated by the onset of loess accumulation on the surface.

The laminations and slightly coarser grain size distribution of the basal capping deposit indicate fluvial deposition. This layer may represent fluvially reworked loess or fine fan material, or low-energy overbank deposits at the tail end of deposition of this terrace. The small thickness and clast size distribution of the unit indicate deposition by a small, low energy flow, rather than a large surface-reworking flow from the major upstream catchment, and thus postdate emplacement of the gravel deposit. As a fluvial deposit this layer potentially violates the OSL burial-age criterion that material be fully exposed to light immediately prior to deposition, and may thus reflect an anomalously old age due to partial bleaching. Our measured age for the oldest definitively aeolian loess deposit is ~ 3 kyr younger, permitting the interpretation that fluvial reshaping of the Q2 surface continued until 16.4 ± 0.5 ka. We thus take 19.1 ± 1 ka as a maximum age for the abandonment of the Q2 surface by the main streams. The offset of all channels by 79 ± 5 m and a maximum formation age of 19.1 ± 1 ka give a minimum slip rate of 4.1 ± 0.4 mm yr⁻¹. A minimum abandonment age of 16.4 ± 0.5 ka indicated by the primary aeolian silt above allows a slightly higher maximum slip rate of 4.8 ± 0.4 mm yr⁻¹.

5.2 93.02°E Ta Si He

At the longitude of 93.018°E, on the west side of the Aksay bend, the SATF forms a distinct, continuous linear scarp along the mountainfront south of Annanba Valley. This sharp, continuous scarp represents the most recent earthquake, well preserved along the fault as reported in *Wang et al.* (2004), *Mériaux et al.* (2005), and *Elliott et al.* (2015). Several large ephemeral streams drain northward across the SATF here in Annanba Valley, carrying large (up to 2 m) clasts of gneiss and recycled boulder conglomerate from the mountains south of the fault. The Ta Si He drainage is the westernmost large north-draining river along this reach of the SATF, occupying the contact between gneissic rock to the east and boulder conglomerate to the west. The conglomerate represents incised basin sediments that have been translated left-laterally from their sources north of the SATF in Xinjiang Province into topographic juxtaposition with the triangular half-graben of Annanba Valley. They are in turn currently being incised and transported northward into this depositional basin.

At the Ta Si He site, the SATF crosses the apex of a coarse alluvial fan complex deposited by the Ta Si river (Fig. 5). From both the east and west, the fault projects in from distinct linear traces along the mountainfront, but across these fan deposits it splays into an en echelon array of right stepping faults. Individually, these faults strike slightly counter-clockwise of the local SATF strike, exhibiting the structural orientation of Riedel shears within the left-lateral fault zone. These en echelon strands are each 70–100 m long and spaced ~10–15 m apart (Fig. 5). The fault strands offset all but the most recent stream deposit and active channel (T0' and T0, respectively). From the active channel, a flight of abandoned alluvial fan surfaces rises to the west (T1–T4). The surfaces occupy distinct levels, separated by >1-m risers, and individually contain microtopographic relief (i.e., bar and swale morphology) of ~1 m.

The terrace levels can be distinguished by elevation and inset relationships. Relative ages are further represented by different depths of loess filling the original channels, and by differing degrees of weathering on boulders exposed in large bars. The T0' surface exhibits mild weathering, but insufficient loess deposition to fill interstitial space among the surface boulders. The T1 surface contains loess that fills pore space among boulders. Boulders on T1 exhibit thorough weathering of their surfaces, forming roughly 2 mm weathering rinds but exhibiting little to no attrition of individual crystals. The T2 and T2' surfaces are thoroughly covered by loess, through which only boulder bars are exposed. The swales contain 40 ± 10 cm of loess as measured in our sample pit #2. This substantial topographic smoothing from the original surface distinguishes these terraces from T1. T2 and T2' are distinguished from one another by a 50 cm difference in elevation. The systematic shift in elevation suggests a difference caused by original surface height rather than subsequent differential deposition of loess. The T2' surface is separated from the next higher surface by a 4 m riser. Upstream of the fault this is the T3/T2' riser. The T3 surface is the most widespread at the site, comprising a vast fan surface with a distinct network of preserved channels, now filled with 50 ± 10 cm of loess. The boulder bars on T3 are composed of up-to-100-cm clasts that have mild coatings of desert varnish. These clasts appear generally half buried in loess, and many exhibit attrition of original smoothed crystalline surfaces over ~50% of their exposed surface area. Downstream of the fault a triangular remnant of a higher surface lies between T3 and T2'. This surface, T4, exhibits extensive desert varnish, and loess infilling has obscured the original channel network.

For the most widespread fan surface, T3, the bar and swale morphology forms a distinct set of offset markers. These piercing lines can be reliably correlated across the fault because they can be traced through multiple small offsets across each en echelon strand (Fig. 5). In particular, we correlate the boulder-loess contacts at the margins of several loess-filled channels on the T3 surface. The best preserved of these features is the easternmost channel margin upstream of the fault; to the west, shepherds have removed the original channel bars to both grade and build a corral and shelter. Nonetheless, remnants of other original swales to the west are preserved downstream of the fault and folded over narrow pushup ridges within the en echelon fault zone. The high quality offset of the easternmost channel margin is 32 ± 4 m. Restoration of both Quickbird imagery and our Total Station topographic contour map by backslip of this amount results in good alignment of the western swales across the fault. The abandonment age of this surface represents a minimum age for the formation of these microtopographic features.

Downstream of the fault an abandoned remnant of an older T4 surface bounds the east side of T3, but this remnant is absent upstream, suggesting it has been completely removed by erosion upstream of the fault on the west side of the river (Fig. 5). A 4 m high east-facing riser separates these old generations (T3 and T4, upstream and downstream, respectively) from the T2' surface. This upper riser of the T2' terrace tread (hereafter referred to as T3/T2') is offset only 19 ± 4 m, in contrast to the 32 ± 4 m offset of the T3 surface, indicating at least 13 m of riser erosion during accumulation of slip in the upper (T3) deposit. The next lower riser, T2'/T2, is marked by a boulder bar of asymmetric height. Downstream of the fault this bar is surrounded by loess deposits on both bounding surfaces, forming merely an east-facing 30-cm-high riser. Upstream of the fault this boulder bar rises 20 cm from T2' and 60 cm from T2. The crest of this boulder bar, correlated across two of the en echelon fault strands, is offset 23 ± 4 m. The T2/T1 riser is offset 22 ± 3 m. Within uncertainty, all three of these risers in between these narrowly separated surfaces appear to have been offset the same amount. This indicates that the 19 ± 4 m offset of the T3/T2' riser must thus have accumulated only after abandonment of the lower (T2') terrace, requiring a lower terrace age interpretation for that offset. As the largest landform and thus most confidently defined piercing line among the lower risers, the T3/T2' riser gives the most reliable offset measurement of these features.

To ascertain the abandonment age of each of the abandoned alluvial surfaces at Ta Si He, we collected amalgamated samples of boulder-tops from each surface's boulder bars for Beryllium-

10 exposure age dating. Samples were carefully selected from smooth, exposed tops of boulders partially encased in loess in order to avoid sites of surface attrition, ensure unshielded exposure to cosmic rays, and reduce the likelihood that the sampled boulder has moved or overturned since deposition. Samples were ground and cleaned, and Beryllium was extracted following the methods described in *Blisniuk et al. (2010)*. An amalgamated sample was also collected from smooth surfaces atop the boulders of the modern channel, in order to measure the average inherited component of Be-10. The $\text{Be}^{10}/\text{Be}^9$ ratios of extracted Beryllium were measured via accelerator mass spectrometry at the Purdue Rare Isotope Measurement (PRIME) lab at Purdue University. Results reported here list 1-sigma analytical errors. Measured Be-10 concentrations and calculated ages are reported in Table 3.

Cosmogenic Be-10 production rate at Ta Si He is calculated to be 37 ± 5 atoms $\text{g}^{-1} \text{yr}^{-1}$ following *Stone (2000)* after *Lal (1991)*, based on the site location of 39.3335°N , 93.0181°E (geomagnetic latitude 29.53°), 3 km above sea level. The Be-10 concentration measured from the modern channel—reflecting the average inherited value within the catchment—is relatively high, at $(1.80 \pm 0.14) \times 10^5$ atoms g^{-1} , or an equivalent date of 4.862 ± 0.4 ka at the calculated site production rate of 37 atoms $\text{g}^{-1} \text{yr}^{-1}$. The relatively high implied inheritance may result from the two-stage depositional history of these clasts, many of which have been eroded from the conglomerates that comprise the “bedrock” on the south side of the fault here. There they may have had a prior exposure history in the now-beheaded alluvial bajada which has been translated left-laterally from its source area to the west (Fig. 3).

The T3 amalgamated boulder exposure date, corrected for average inheritance measured in the modern stream, is 14.1 ± 0.5 ka. The dates calculated for T2' and T1 overlap within error, at 4.2 ± 1.7 ka and 5.0 ± 0.8 ka respectively. These results corroborate the inference from minimal differences among the elevations and morphologic characteristics among these surfaces that they were deposited and abandoned within a short time of one another. The dates are also consistent with the observation of similar offset magnitudes of the three upper risers that respectively bound these surfaces (Fig. 5).

To corroborate these Be-10 exposure dates, we sampled the bases of the channel-filling loess deposits on both T3 and T2'. We expect OSL burial dates from these samples to represent the minimum abandonment age of each respective surface. In fact we interpret these loess burial ages to more closely represent the age of surface stabilization, as surface boulders may have been

mobilized and rearranged by heavy flows before, but not after, loess began accumulating on the surface. Sample information and analytical results are presented in Table 1. On T2', the loess date closely corroborates the boulder exposure age obtained from Be-10 dating, at 4.7 ± 0.2 ka. Two pieces of charcoal collected from 15 cm above the gravel-loess contact on the T2' surface give calibrated radiocarbon dates of 2805 ± 32 a and 2796 ± 31 a (Table 2). Three more charcoal fragments from ~25–30 cm above the base of the loess return radiocarbon dates of 2580 ± 82 a, 2585 ± 72 a, and 2589 ± 65 a; a sixth charcoal fragment from 22 cm above the base returns a date of 1845 ± 149 a. These radiocarbon samples come from horizons at approximately one to two thirds of the loess depth within the pit (loess depth varies by 15–20 cm over large clasts on the rough gravel deposit surface), and collectively provide minimum age bounds on the onset of loess deposition, corroborating the Be-10 and OSL dates. The OSL burial date obtained from the base of the 50-cm deep loess channel-fill on the T3 surface is 7.8 ± 1.6 ka. This date is substantially younger than that obtained from Be-10 measurements of amalgamated bouldertops on this same surface. Bouldertop exposure ages represent the full duration of surface emplacement, and may include unaccounted-for inheritance from their pre-depositional histories, whereas OSL ages represent abandonment of the surface. Therefore the OSL date provides the age of accumulated offsets of morphological features. Charcoal fragments from shallow depths in the loess deposit have radiocarbon dates of 1570 ± 27 a and 1956 ± 44 a (Table 2), offering bare minimum dates to corroborate earlier establishment of the capping deposit.

The slip rate at Ta Si He can be ascertained based on four different offset markers. With an offset of 32 ± 4 m and a minimum abandonment age of 7.8 ± 1.6 ka, the T3 surface indicates a maximum Holocene slip rate of $4.1^{+1.7}/_{-1.1}$ mm yr⁻¹. Taking the T3 boulder exposure age of 14.1 ± 0.5 ka as a maximum for the stabilization age of the channel morphology on this surface gives a minimum slip rate of 2.3 ± 0.4 mm yr⁻¹. The 19 ± 4 m offset of the T3/T2' riser postdates both emplacement and abandonment of the T2' surface, dated at 4.7 ± 0.2 ka. This marker gives a slip rate of $4.0^{+1.1}/_{-1.0}$ mm yr⁻¹, matching, within error, the higher of two slip rates obtained from offset of the higher surface.

5.3 93.28°E Tuboshu

As the SATF attains a more easterly strike of $\sim 90^\circ$, it forms a high-altitude fault-line valley along which flows the upper reach of the Annanba River. At 93.282°E 39.232°N, ~ 10 km west of the SATF's intersection with a major normal fault that branches northeastward into the Altun Range, a series of alluvial fans are offset by the fault at the Tuboshu site. At the mouth of one drainage the deformed fans exhibit clear conical morphology both up- and downstream of the fault, permitting reconstruction of the original fan shape to obtain fault displacement since the fan's formation.

At this site a south-flowing stream crosses the SATF and has deposited a series of ~ 50 -m-wide alluvial fans (Fig. 6). The modern stream occupies a narrow channel on the west side of the drainage, where it has incised older generations of fans sourced in the same catchment. 80 m downstream of the fault, the channel opens and occupies a network of ephemeral streams forming the T1 fan surface (Fig. 6a). The next oldest abandoned fan, T2, emanates from a point upstream of the fault, exhibiting quasi-conical morphology both up- and downstream of the SATF. Upstream of the fault this morphology is evident in arcuate elevation contours from a differential GPS survey, but is truncated by the abrupt linear fault scarp across which terrain steps downward 15 to 20 m (Figs. 6 & 6). Downstream of the fault the fan morphology is similarly clearly defined by arcuate contours and additionally by divergent microtopographic depressions (small rills) oriented perpendicular to elevation contours on the loess-covered fan surface. Together these topographic markers define an alluvial fan whose apex is offset 19 ± 5 m from the corresponding apex upstream (Figs. 6 & 6). Two sequentially older beheaded fan lobes are defined by arcuate contours concentric around different points to the east. The large fan whose apex is farthest from the upstream drainage is labeled T2', and the smaller intervening deposit along the boundary between T2' and T2 is labeled T2s. The distinction among these units is morphological. T2s is a smaller geomorphic feature that does not exhibit the same broad arcuate contours of the large fans on either side.

The offset of T2 across the fault is corroborated by two related geomorphic measurements. The first is derived from mapping and field measurement of the offset fan apex. The fan apex can be characterized in map view as the line along which drainage directions parallel the upstream channel orientation, perpendicular to the fault (Fig. 6). Uncertainty in the position of the fan apex arises from the gentle curvature of the fan, and is characterized by field assessment of farthest

east and farthest west possible apex positions. The second measurement derives from reconstruction and alignment of the concentric topographic contours that represent these conical fan remnants. We use the elevation contours of a dGPS-derived triangulated surface. These contours can be approximated by concentric rings about an abstract point that represents the head of the fan (Fig. 7). Presuming purely left-lateral motion of the fault, the east-west difference in the center position of the up and downstream contours represents fault slip since stabilization of the fan. Uncertainties in these values are based on the range of fan head positions for which concentric circles sub-parallel topographic contours, minimizing the angle between synthetic contours and observed (Fig. 7). Both of these measurements indicate offset of 19 ± 5 m. Restoring the apex of T2' back to the same upstream drainage reveals an offset of 38 ± 10 m (Figs. 5 & 6).

The T2 fan surface is covered by 130–140 cm of loess. As with other geomorphic features in the region, the loess represents aeolian silt that could only have accumulated in the absence of regular fluvial flows across the surface; thus the onset of loess accumulation provides a minimum bound for the abandonment and stabilization age of the geomorphic surface. We excavated a pit into the T2 surface near the downstream apex of the fan. We collected a loess sample from the base of the capping loess deposit, 5 cm above the gravel-loess contact, at 135 cm depth. The OSL burial date of this sample is 10.8 ± 0.6 ka (Table 1).

The fan abandonment age of 10.8 ± 0.6 ka is interpreted to represent the minimum time since stabilization of the conical landform that we observe offset 19 ± 5 m by the SATF. Together these data indicate a maximum Holocene slip rate of 1.8 ± 0.6 mm yr⁻¹ at this reach of the SATF.

5.4 94.42°E Dangjin Shankou

East of the 25° double-bend, the SATF reattains a strike of $\sim 071^\circ$ but is only rarely expressed as a linear scarp in Quaternary geomorphic surfaces. Within the bend, at 39.219°N 93.645°E, *Elliott et al.* (2015) identify an undeformed Pleistocene alluvial fan that overlaps the fault, with no vertical nor horizontal offset, suggesting that this central portion of the SATF has not ruptured in the Holocene. Though the entire SATF is topographically evident as a linear break in slope between rugged bedrock to the north and alluvial fan deposits to the south (e.g., Fig. 2), we have identified only one drainage along the reach of the fault east of 93.8°E in which alluvial fans

cross the fault and have measurable left-lateral offsets. At this site, 6 km east of Highway G215 where it enters Dangjin Mountain Pass (“shan kou” in Mandarin), the major mountainfront strand of the SATF projects across a deeply loess-covered alluvial fan complex, in which incised channels s1, s2, and s3 are left-laterally offset across the surface trace of the fault as described below (Fig. 8). We mapped the geomorphology of the site on 60-cm Quickbird imagery and quantified the topography with a Total Station survey of 555 points covering an area of 160×160 m. We use the Total Station survey to measure geomorphic offsets and to inform our interpretation of surface margins and incised channel geometries (Fig. 8).

The SATF Dangjin Shankou site contains two 2.5-m-deep channels (s2 & s3) that have been incised into an abandoned alluvial fan (T2) and offset by the SATF. The surface of T2 lies ~ 12 m above the thalwegs of the main modern channels sourced in upstream catchments and is heavily smoothed by a 150-cm-thick capping loess deposit, measured in natural exposures on its incised eastern margin and in the ~ 1.5 m deep pit we excavated for geochronologic sampling. The margins of the surface are highly rounded except where incised by the two narrow channels (Fig. 8). The base level of these channels is the axial stream bounding this and a neighboring fan complex. Both of these channels are distinctly offset 9 ± 2 m across the SATF (Figs. 7 & 8). Downstream of the fault the channels deepen to 3.5–4.0 m where the T2 surface is locally uplifted in a narrow fault-parallel fold (Fig. 8), but the channel thalwegs are undeformed.

Inset on the west side of T2 is a lower, flatter abandoned alluvial surface, T1, which stands 3.5 m above the modern channel. The loess depth on this surface is 70 cm as measured in a pit excavated on its flat central portion. The riser between T1 and T2 is distinct and sharp downstream of the fault, but upstream of the fault, low curvature of the T2 surface makes the projection of the riser unidentifiable within 20 m of the fault (Fig. 9). A range of possible projections permits apparent sinistral offset of this riser ranging from 0 to 12 m. We hence view this riser as a poor marker of fault offset. A shallow channel (s1) incised into the T1 surface appears left-deflected at the fault (Fig. 8), but sinuosity up- and downstream of this potential offset cast uncertainty onto its origin; its precise geometry may be further modified by a herd path that follows the trace of the fault. The T1 surface lacks the folding observed in T2, indicating that deposition of the T1 deposit postdates this deformation. The channels incised into T2 exhibit the only definitive left-lateral offsets at this site, so the age of this incision gives the time-averaged slip rate.

We excavated and sampled the T1 and T2 surfaces in order to constrain the abandonment age of each (Fig. 8). The gravel deposits forming these surfaces are composed of small (<5 cm length), highly elongate clasts derived from the local bedrock schist. As with other sites reported here, we argue that the best constraint on abandonment age is the onset of loess accumulation, so we collected multiple OSL samples from each pit to constrain this age and verify stratigraphic consistency (Supplemental Fig. S1, Table 1). Loess from the base of the T2 pit (sample L31) returns a burial date of 75.2 ± 8.4 ka, the oldest of any geochronologic date we obtained in this region. Further constraint on the age of this surface comes from sample L32, 50 cm above the base of the loess cap, at 100 cm depth from the surface. Sample L32 returns a date of 9.4 ± 1.2 ka. Dates from the lower T1 surface provides further stratigraphic constraint on the bare minimum abandonment age of the older surface. Sample L22 from the base of the T1 loess cap (70 cm depth) returns a date of 10.7 ± 0.8 ka, and sample L21, at 35 cm depth, returns a date of 6.9 ± 0.4 ka. A piece of charcoal collected from 40 cm depth, just below OSL sample L21 has a calibrated radiocarbon date of 7.1 ± 0.3 ka (Table 1), stratigraphically consistent with the OSL results from this deposit.

The two offset channels in the T2 surface are incised through the fault-parallel fold, indicating their antecedence to the structure, predating fault deformation but postdating abandonment of T2. The folding in turn predates deposition of T1. Thus the abandonment age of T2 gives the maximum age for the left-lateral fault offsets recorded by these channels, and the abandonment age of T1 provides a minimum. These ages are constrained by the burial dates at the base of the surface-capping loess deposits.

The exceptional 75.2 ± 8.4 ka date of sample L31 from the base of the T2 loess may be due to only partial bleaching during the sample's deposition, or to a radioactive dosage source that was not captured by our dose rate sampling. Stratigraphically, sample L32, from higher in the loess deposit on the T2 surface, was buried long after the abandonment of the T2 surface, making its date of 9.4 ± 1.2 ka an absolute minimum for the onset of incision of the two channels s2 and s3. The burial date of L22 from the base of the T1 superjacent loess indicates that abandonment of even the inset T1 surface predates 10.7 ± 0.8 ka. The apparent age of 75.2 ± 8.4 ka at the base of the T2 loess is highly suspect as an anomalously old age compared to similar loess-mantled surfaces throughout the region, especially compared with the 9.4 ± 1.2 ka age at half its depth. At face value, this pair of ages suggests a marked increase in loess deposition rate in the Holocene,

or an undetected hiatus or truncation within the loess. This may be compatible with interpretations from regional studies that find increased loess deposition after the last glacial maximum (e.g., *Lehmkuhl et al.*, 2000; *Owen et al.*, 2006; *Sun et al.*, 2007).

We use the stratigraphically consistent dates from the T1 surface and the higher T2 sample to calculate a maximum slip rate at this site. The 9 ± 2 m channel offsets, paired with a minimum incision age that predates folding and in turn deposition and abandonment of T1 (10.7 ± 0.8 ka) allow a maximum SATF slip rate of 0.8 ± 0.3 mm yr⁻¹ at the longitude of 94.42°E. The maximum credible T2 loess age of 75.2 ± 8.4 ka indicated by sample L31 yields a slip rate of just 0.1 ± 0.05 mm yr⁻¹.

5.5 Annanba Valley Fault

At approximately 92.96°E, between the Xinjiang Border and the Ta Si He sites, an oblique left-normal fault branches northward from the SATF with a strike of 060° and dip of 65° SE. This fault forms the linear northwestern margin of the triangular half-graben that is Annanba Valley (Fig. 2c; Fig. 3), and is herein named the Annanba Valley fault (AVF). The AVF juxtaposes Quaternary basin-fill conglomerates in its hangingwall against quartzites and lithified (older basin-fill) conglomerates in its footwall to the north. This lithologic and topographic boundary is traceable northeastward for 20 km to within 500 m of the NATF. At its northeastern end, nearest the NATF, undeformed Quaternary gravels overlap the fault.

The topographic relief across the AVF decreases eastward (Fig. 3), from 500 m elevation difference between range crest and basin floor in the west to <100 m in the east, where finally the elevation difference reverses where the AVF is evidently inactive. Despite its conspicuous topographic signature, the AVF forms few small scarps in Quaternary geomorphic features. In part, tectonic scarps may be overprinted or obliterated by fluvial deposits along a tributary of the Annanba River that parallels the fault along the northwest margin of Annanba Valley (Fig. 3).

Where a large north-flowing alluvial fan crosses the AVF at 93.046°E, the fault forms uphill-facing scarps that offset at least three generations of alluvial deposits (Fig. 10; further described in Supplemental Material). Deep incision into this fan crosses through the fault zone, exposing a striated fault plane with a rake of 35° implying a left- to normal-slip ratio of ~2:1 (Fig. 10b). Exposed vertical offsets of the surface gravel lag deposits are 1.75 and 0.5 m, respectively, of

alluvial surfaces that postdate 3.7 ± 0.5 ka (Table 1, Supplemental Material). The difference in offset between these adjacent deposits requires at least two different slip events in this time period (Supplemental Material).

6 Discussion and Implications

6.1 Summary of results

The observations presented here show that as the SATF traverses the Aksay bend, its multi-event averaged slip rate drops from ~ 4 mm yr⁻¹ to less than 1 mm yr⁻¹, diminishing to effectively zero slip rate along a reach of fault that exhibits no lateral slip in the Holocene (*Elliott et al.*, 2015). Figure 11 shows graphically the sinistral slip rates we have determined along the SATF at the Aksay restraining double-bend. The results are tabulated in Table 4. On the west side of the bend, at $\sim 93.0^\circ\text{E}$, the SATF slips at 4.1 ± 0.4 mm yr⁻¹, corroborated by another nearby slip rate of $4.0^{+1.7}_{-1.1}$ mm yr⁻¹. As the fault begins to bend, the Holocene slip rate declines to 1.8 ± 0.6 mm yr⁻¹ at $\sim 93.3^\circ\text{E}$. On the east side of the bend, at $\sim 94.3^\circ\text{E}$, the SATF slips at as little as 0.1 ± 0.05 mm yr⁻¹ and no more than 0.8 ± 0.3 mm yr⁻¹. Because at the Aksay bend the Altyn Tagh comprises two parallel fault strands, our rates are expected to represent only a fraction of the full fault zone rate calculated geodetically. Nonetheless, the observed gradient in slip rate reflects real seismic behavior of an individual fault, lending insight to the physical processes that control rupture propagation.

6.2 Slip Rates Reflect Earthquake Behavior

The observed slip-rate gradient presented here matches the slip accumulation predicted by numerical modeling of a bend that halts ruptures (*Duan and Oglesby*, 2005, Fig 1), as this one did in its most recent earthquake, which had a magnitude of likely around $M_w 7.8$ (*Elliott et al.*, 2015). Because the offsets used to calculate these long-term slip rates total between 9 and 79 meters, and occupy sites near smaller offsets, they each must represent multiple (in some cases many) individual earthquakes. Average slip in the most recent event on this reach of the fault was on the order of 5 m (*Washburn et al.*, 2001; *Elliott et al.*, 2015), and smaller more recent rupture

of the western ATF exhibited only <1 m of left slip (*Li et al.*, 2016). In other continental strike-slip ruptures around the world, coseismic slip has only rarely exceeded 10 m (*Baljinnyam et al.*, 1993; *Rodgers and Little*, 2006; *Avouac*, 2015; *Barnhart et al.*, 2015; *Zinke et al.*, 2014; *Hollingsworth et al.*, 2017; *Hamling et al.*, 2017; although some of these are disputed; see, e.g., *Lasserre et al.* 2005; *Klinger et al.*, 2005), and seldom if ever averages as much (e.g., *King and Wesnousky*, 2007). Thus our measured offsets are likely to represent no fewer than two earthquakes and in most cases significantly more.

Although we cannot trace the extents of earlier surface ruptures than the most recent, the comparison of our gradient in long-term slip rate with the results of physics-based numerical modeling lends insight into the constituent earthquakes that have produced these average slip rates. The gradient we observe may arise from either a) the consistent locus of taper near the tip of successive fault ruptures, or b) a progressively smaller number of ruptures reaching beyond a certain distance into the bend (Fig. 11c). Although no single-event offsets are measurable within the easternmost 10 km of the most recent surface rupture, its slip distribution does not exhibit a significant taper in offset toward the east that would match the observed gradient in slip rate. Nonetheless, coseismic slip distributions are generally taken to have quasi elliptical forms, requiring some finite distance to reach from full fault slip to 0 at the rupture tip (e.g., *Scholz et al.* 1993; *Dawers and Anders*, 1995; *King and Wesnousky*, 2007). Divergence from a strict elliptical form is common and may be controlled by structural and dynamic effects, which modulate the location and steepness of coseismic slip gradients in individual ruptures (e.g., *Biasi and Weldon*, 2006; *Oglesby*, 2008). Hence, a combination of the end-member models of varying rupture termini and varying coseismic slip gradients may lead to the observed accumulation of slip (Fig. 11c).

6.3 Lack of Connectivity Between SATF and NATF

One possible explanation for the decline in slip rate on the SATF could be the gradual transfer of slip onto the NATF, however geomorphic, structural, and paleoseismological data show that the candidate connecting structures do not coseismically bridge the two main faults. Two oblique left-normal faults branch from the SATF toward the NATF on the west side of the bend (Fig. 2). The first, the AVF, branches off *between* the Xinjiang border site and the Ta Si He site, which

have essentially the same Holocene left-lateral slip rate within uncertainty. Geomorphic expression of the AVF decreases northeastward until it approaches the NATF within 500 m; however, here it is overlain by undeformed fan deposits and exhibits extreme changes in strike that suggest it is not currently active as a throughgoing fault. The second oblique-normal fault branches from the SATF east of the Tuboshu site, and while it kinematically must absorb some of the left-slip, it bends into the mountain range and its geomorphic expression vanishes before meeting the NATF.

Furthermore, where we have investigated an exposure of the AVF (§5.5), the two events that we can distinguish which occurred since abandonment of the older alluvial deposit before 3.7 ± 0.5 ka represent a somewhat lower recurrence rate relative to others established along the main SATF, which hosts events within this region every 700–1100 years (*Washburn et al.*, 2001). The maximum left-slip in each event, 1.5 m and 1 m, respectively, is much lower than any values measured along the most recent SATF rupture and is compatible with an event of only ~ 20 km length, the total length of the AVF.

Significantly, the evident coseismic rupture trace within the field area (*Elliott et al.*, 2015) also shows that rupture—at least in that most recent event—proceeded along the straighter course of the SATF past these branching oblique-normal faults. Detailed mapping indicates that the most recent rupture of the SATF did not propagate/branch onto the AVF, and thus they do not always fail simultaneously. Nonetheless, none of those Holocene ruptures have propagated beyond 93.53° , where an undeformed Pleistocene fan overlaps the fault (*Elliott et al.*, 2015). The displacements observed at the Dangjin Shankou site (§5.4), east of the bend, postdate the age of this undeformed fan in the central section of the Aksay bend, and thus must result from a separate rupture of the eastern portion of the fault.

6.4 Implications for Earthquake Mechanics

As both these slip rates and prior rupture mapping show, direct linkage along a discrete fault cannot fully explain the transfer of slip from the SATF to the NATF on the west side of Aksay bend. Furthermore, geomorphic evidence shows that rupture preferentially propagates into the bend on the SATF, preferring this more mature and colinear branch to the Annanba Valley fault. Propagation of most of these ruptures falters, however, by the time they reach the middle of the bend where the SATF is inactive in the Holocene. The decrease in slip rate along the SATF, in

other words, cannot be explained by transfer of slip onto discrete structures that intersect the fault, but corresponds instead to the change in strike as the fault curves through the double-bend. Numerical modelling of ruptures with this fault geometry indeed predicts this decline in accumulated slip, with a bend of this degree halting most ruptures (*Duan and Oglesby, 2005; Lozos et al., 2011; Fig. 11c*).

Residual stresses at the tips of prior ruptures may enable seismic failure along reaches of fault that would be unfavorable for rupture in a uniform regional stress field (*Duan and Oglesby, 2005*). Thus the seismic history of a fault imparts evolving stress heterogeneities that are likely to modulate the extents of subsequent ruptures, as found experimentally by *Kato et al. (1999)* and inferred by *Schwartz et al. (2012)* on the Denali fault. This multi-event stress evolution represents a secondary factor controlling the length of ruptures at a fault bend and may explain finite slip rates beyond the center of the bend on the SATF. Alternatively, the SATF east of the bend ruptures independently of the SATF to the west. Further study of the earthquake history within the bend is required to discriminate what proportion of the earthquakes here overcome this geometric barrier.

7 Conclusions

We report a systematic along-strike decline in slip rate of the southern strand of the Altyn Tagh Fault where its most recent rupture terminated at the Aksay bend and stepover (93–94.5°E longitude). The slip rate on this strand of the fault system declines from $4.1 \pm 0.4 \text{ mm yr}^{-1}$ in the west (at 93.0°E), corroborated by two adjacent slip rate sites, to $1.8 \pm 0.6 \text{ mm yr}^{-1}$ 30 km farther into the bend (93.3°E), and finally down to $0.8 \pm 0.3 \text{ mm yr}^{-1}$ on the east side of the double-bend (at 94.3°E). This gradient reveals little transmission of slip through the bend along the SATF, which attains a strike that both modeling (*Duan and Oglesby, 2005; Lozos et al., 2011*) and prior observations (*Elliott et al., 2015*) show halts propagating rupture. The offsets of ~ 10 to ~ 80 m considered here over Late Quaternary timescales reflect multiple slip events. Considering coseismic slip in the most recent event on the order of 5 m (*Washburn et al., 2001; Elliott et al., 2015*) and large strike-slip earthquakes rarely exceeding 10 m of slip, these offsets represent between two and a dozen individual earthquakes, implying that the gradients in time-averaged slip rate reflect real systematic behavior of individual ruptures. The disparity in the SATF's Holocene average slip rate between the west and east side of the Aksay bend indicates that the

termination of surface ruptures within the bend repeats through multiple seismic cycles. Thus our observations of fault slip rate agree with model predictions that ruptures terminate on the highly misoriented portion of this restraining double-bend. Low but finite slip rate on the eastern end of the SATF, beyond the Aksay double-bend, suggests that the bend does not completely extinguish slip along the fault, although it evidently inhibits individual ruptures. We suspect that evolving stress heterogeneities may enable the propagation of ruptures that would otherwise be impossible through the bent reach of fault. Specific assessment of seismic hazard in such a setting requires constraint on the proportion of ruptures that successfully navigate the bend, which may give insight into the evolution of stresses at a major geometric barrier. This points the way towards future assessments of earthquake hazard using an integrated, physics-based approach that assimilates information from fault geometry, spatially variable slip-rate, and recent paleoseismic history.

Acknowledgments

This work was supported by the US National Science Foundation [grant number EAR-1050060], The National Science Foundation of China [NSFC grant number 41225010], and through an NSF Graduate Research Fellowship to A.E. We thank Marie-Luce Chevalier and an anonymous reviewer for very thorough and constructive reviews of the manuscript. We would like to thank Ren Zhikun, Yu Junjie, and Li Yanfeng for assistance in the field, as well as driver Wu Ye for multiple years of reliable logistics. We would also like to acknowledge George Hilley, Kim Blisniuk, Marie-Luce Chevalier for assistance with Beryllium-10 sample processing; Chen Jie, Qin Jintang, Yang Huili, and Wang Wei for assistance with luminescence dating, and John Southon and the UCI KeckCCAMS laboratory for radiocarbon dating.

Figures

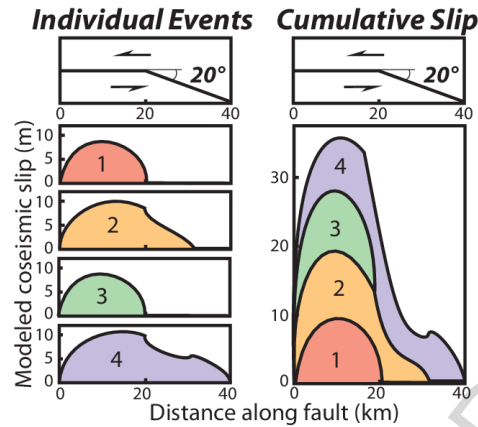


Figure 1: Modeled slip distributions for multiple earthquake cycles on a bent fault, from *Duan and Oglesby (2005)*. Top panels show map of modeled fault. Residual shear stresses from earthquakes 1 and 3 allow the bent fault segment to rupture in earthquakes 2 and 4. Residual stress from earthquake 2 promotes a spike in slip and further propagation of earthquake 4 into the bent segment. Although the entire fault ruptures in this sequence, both the frequency of events and slip per event decrease into the bend.

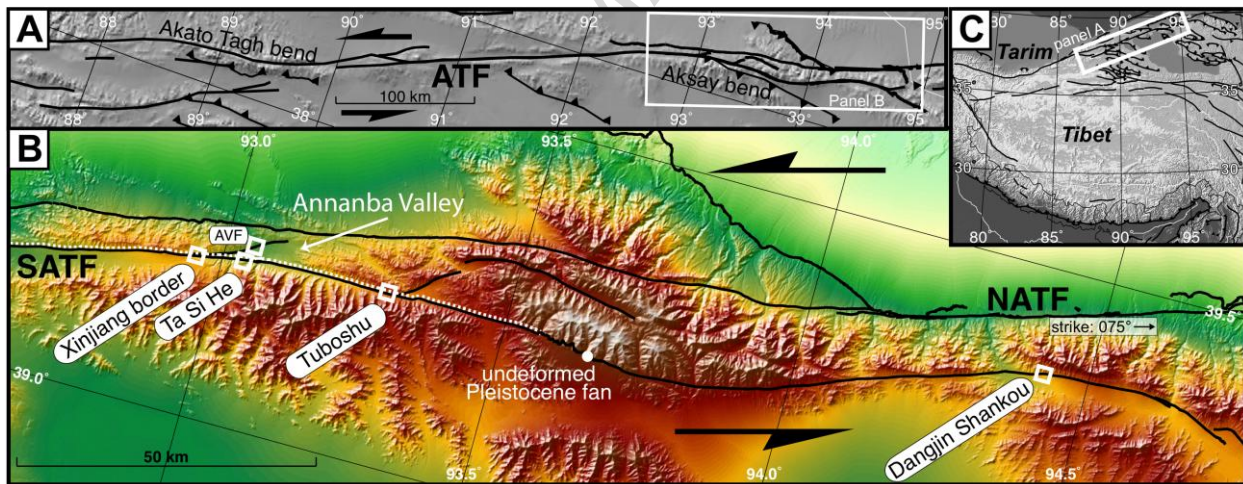


Figure 2: Aksay bend location map. A) Central and Eastern Altyn Tagh fault and major adjacent structures on hillshaded elevation map. Major restraining bends labeled. B) Map of fault geometry and topography at Aksay bend on the eastern Altyn Tagh Fault. Southern (SATF) and northern (NATF) faults labeled. SATF continues to west; NATF continues to east, as shown in Panel A. Portion of fault with dotted line beside represents reach that ruptured in the most recent event, after Elliott et al. (2015). Locations of four slip rate sites presented in this paper labeled. C) Index map of ATF & Aksay bend location relative to Indo-Asian collision zone and Tibet-Qinghai Plateau.

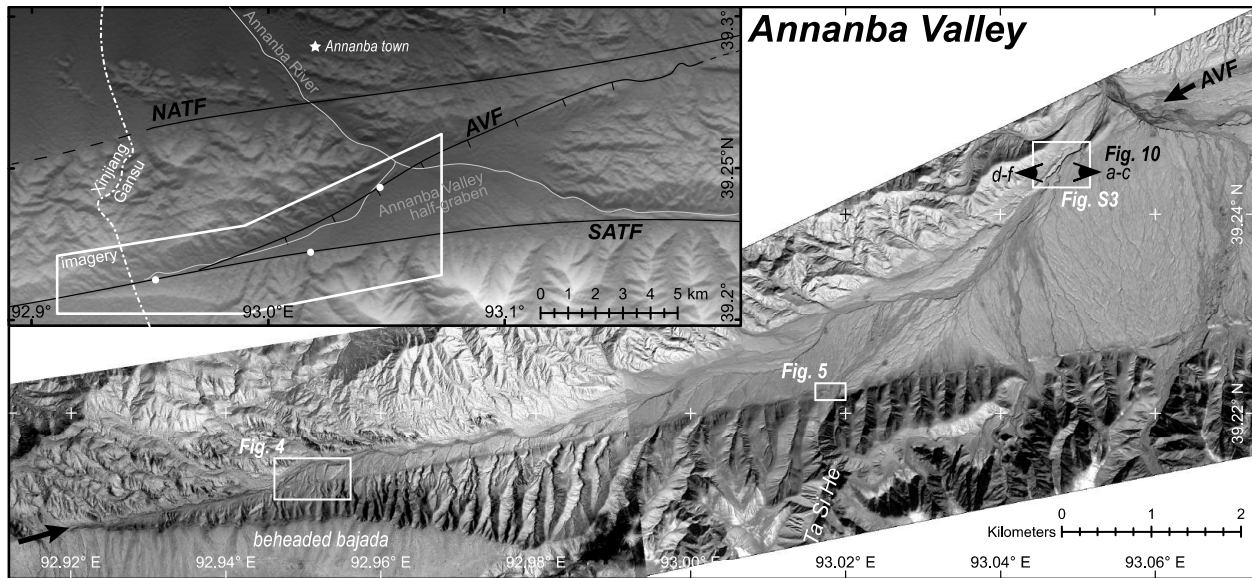


Figure 3: Elevation map & DigitalGlobe Quickbird 60-cm imagery of Annanba Valley / half-graben on the west side of Aksay bend. Locations of the “Xinjiang Border” site, Ta Si He, and the Annanba Valley Fault exposure indicated as white dots, with their respective figure numbers labeled on the imagery. Note that the AVF intersects the SATF between our two western SATF slip rate sites.

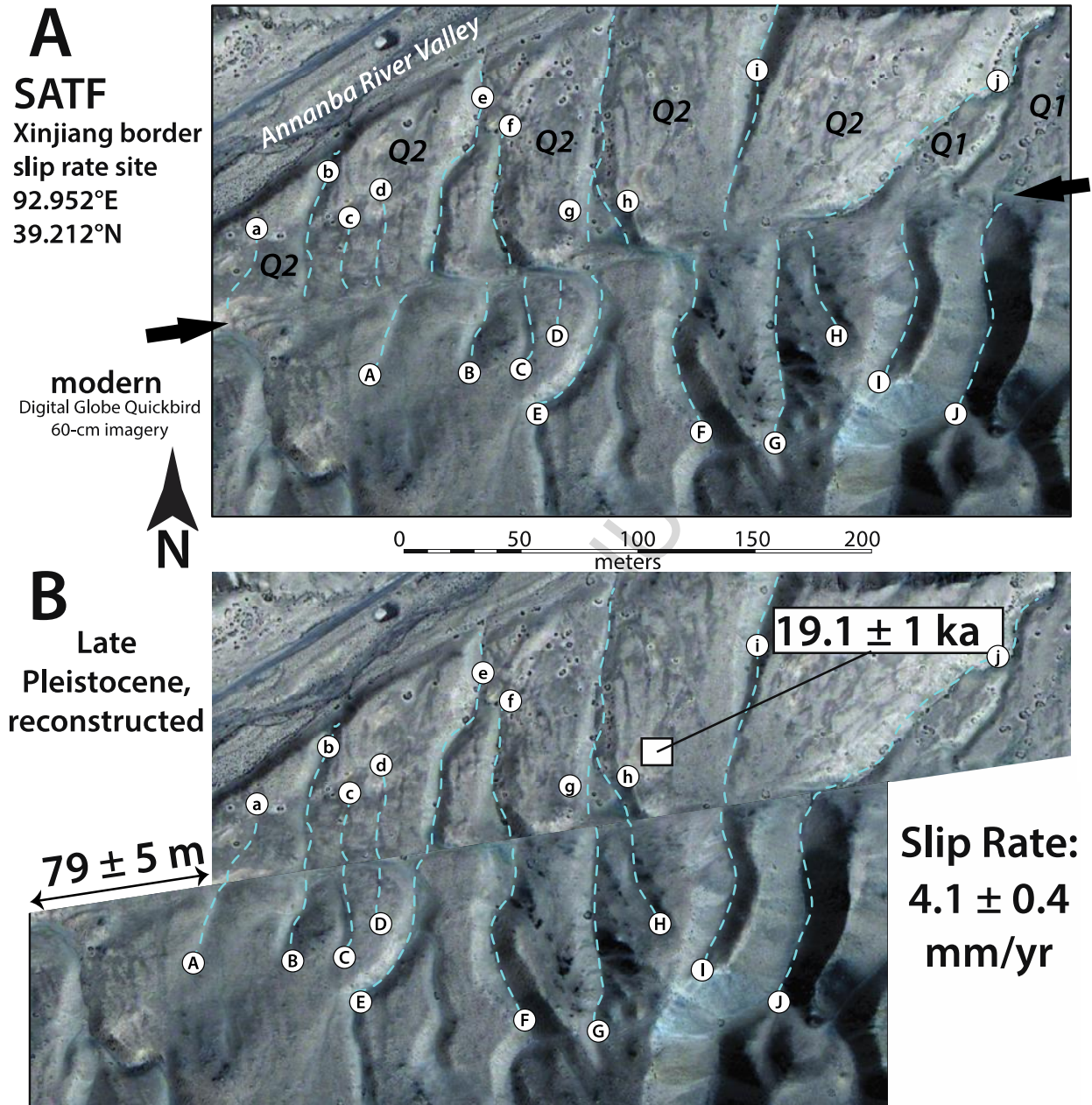


Figure 4: SATF Xinjiang border site reconstruction. Dashed blue lines (labeled capital A-J upstream, lowercase downstream) represent surveyed thalwegs of channels incised 4-8 m into abandoned alluvial surface. Restoration of deflections results in mismatch of channel depths and cross-sectional areas; restoration back two drainages aligns all ten channels with correspondingly sized channels upstream. Alignment of all channels indicates that incision into the abandoned surface was synchronous, at least with respect to the accumulation of offset. Fault slip recorded by these channels postdates abandonment of the surface at 19.1 ± 1 ka as dated by OSL from the base of the overlying loess.

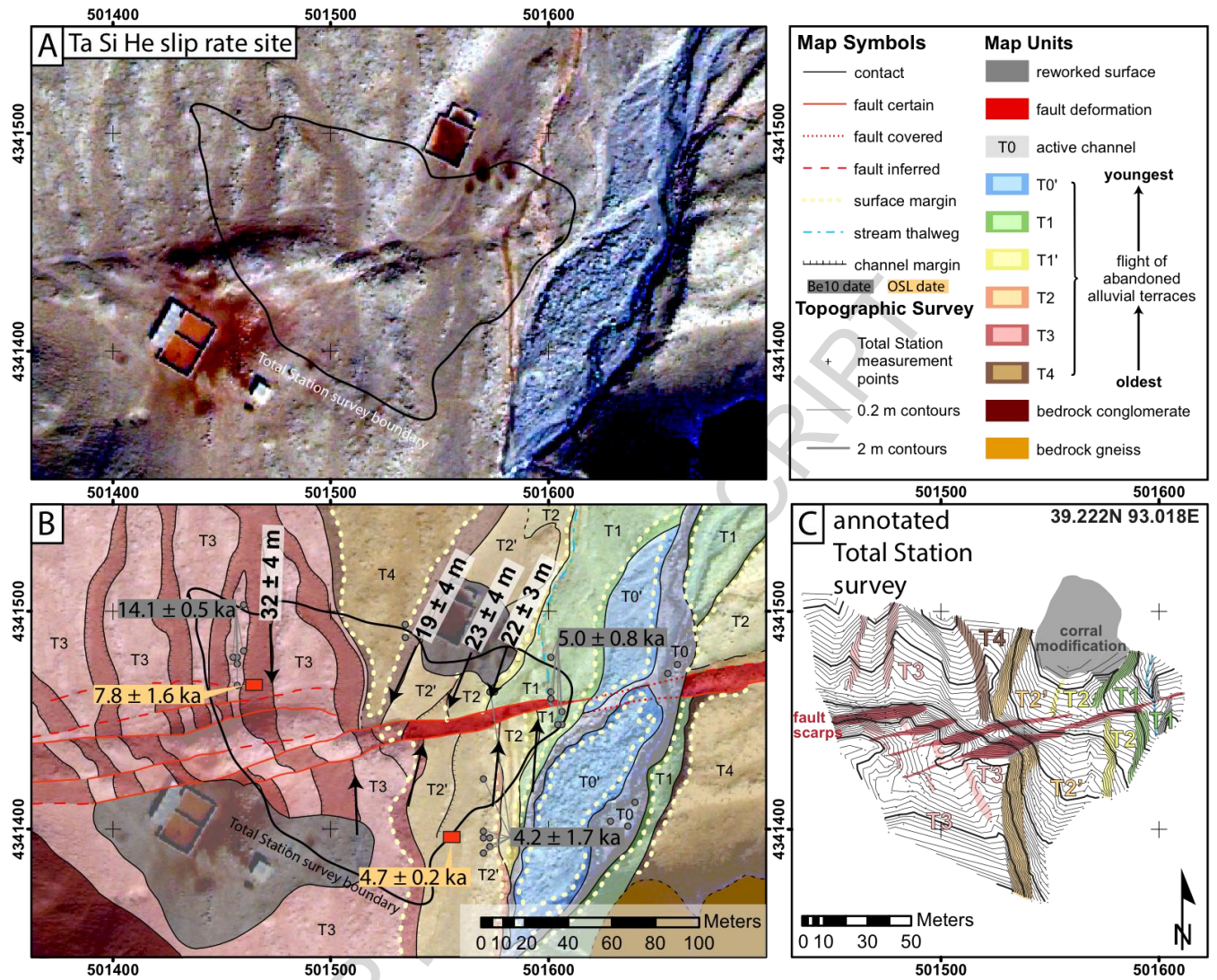


Figure 5: Ta Si He site data. Map, survey, and geochronologic constraints shown; described in the text.

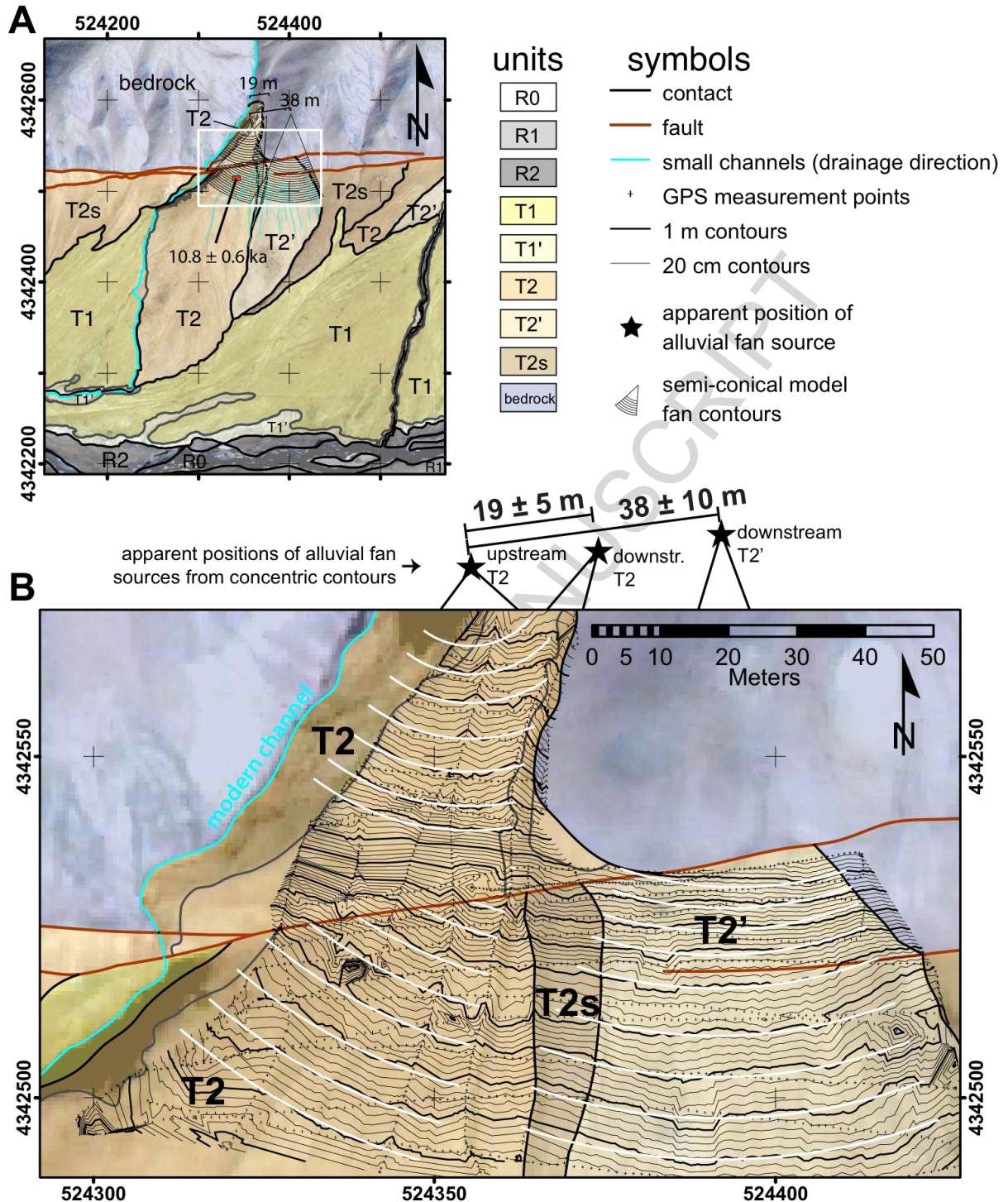


Figure 6: Offset alluvial fans at the SATF Tuboshu site. a) small-scale site map showing that several generations of fans have been translated laterally from their source drainage. Note that T2' appears to emanate from a steep bedrock hillslope. Conical fans are also defined by divergence of drainage directions in small channels across their surfaces, which are oriented sub-perpendicular to concentric circles that define the fan apex. b) larger scale map of TuBoShu alluvial fans. Small fans across the SATF exhibit conical morphology that is truncated by offset across the fault. The offset is characterized by displacement between origins of concentric contours as defined by differential GPS surveys.

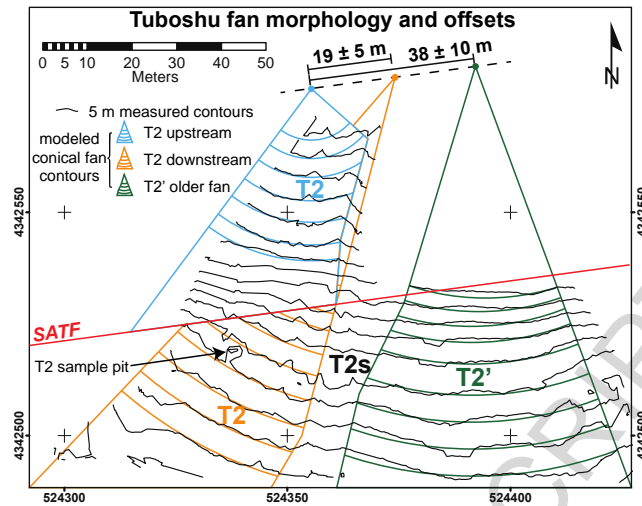


Figure 7: Simplified map of dGPS fan survey at Tuboshu site showing 5 m contours. Synthetic contours represented as concentric arcs for each mapped deposit, radiating from apparent upstream sources as identified by mapping.

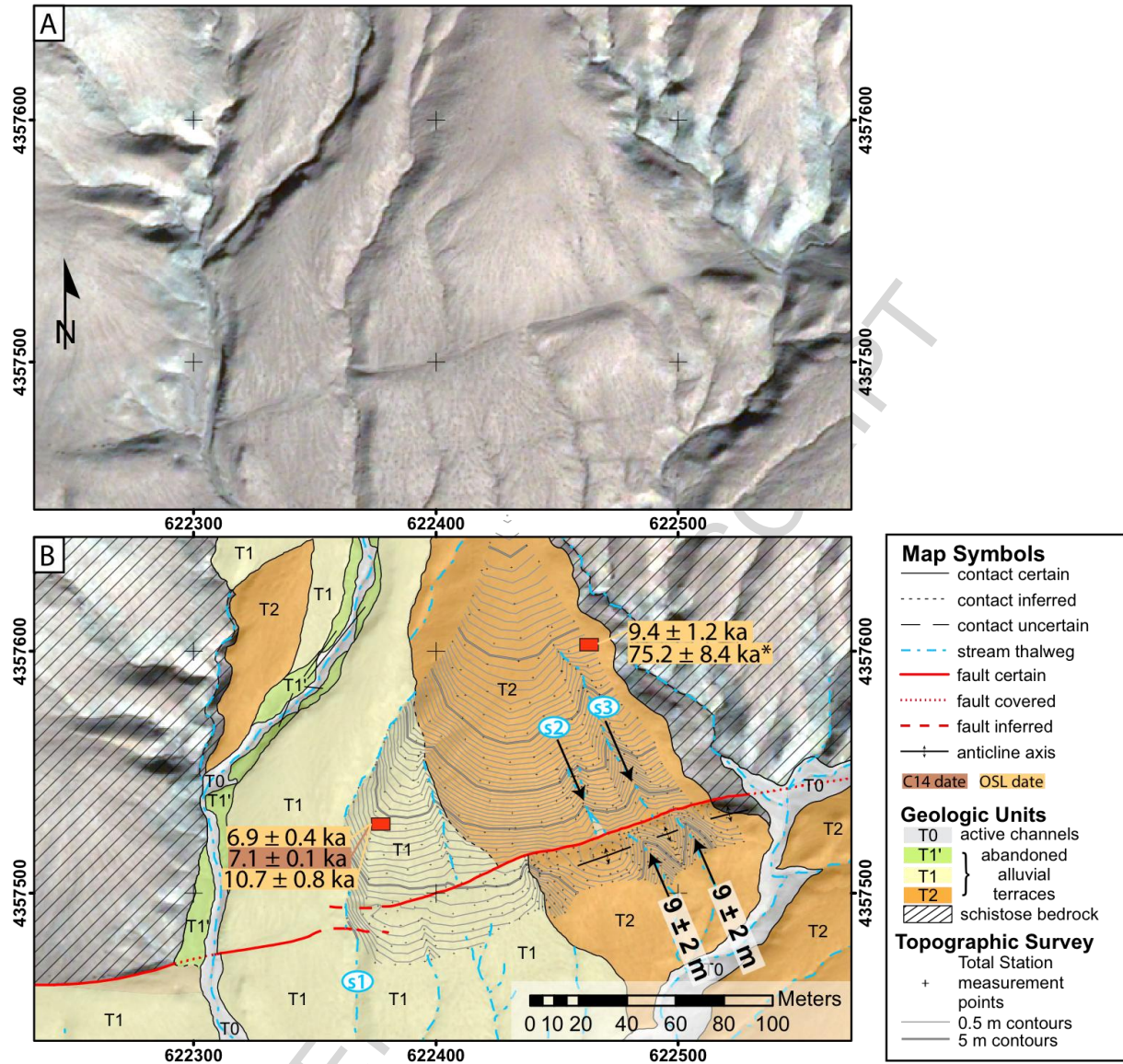


Figure 8: SATF Dangjin Shankou site map & geomorphic interpretation. A) bare 60-cm DigitalGlobe Quickbird imagery, March, 2003 scene. UTM zone 46N. B) interpreted geomorphic map showing abandoned alluvial surfaces, stream thalwegs, fault trace, sample locations and dates (stacked according to depth from surface), and topographic survey contours. See text for description and explanation of geochronologic data. * indicates regionally anomalous loess date omitted from interpretation.

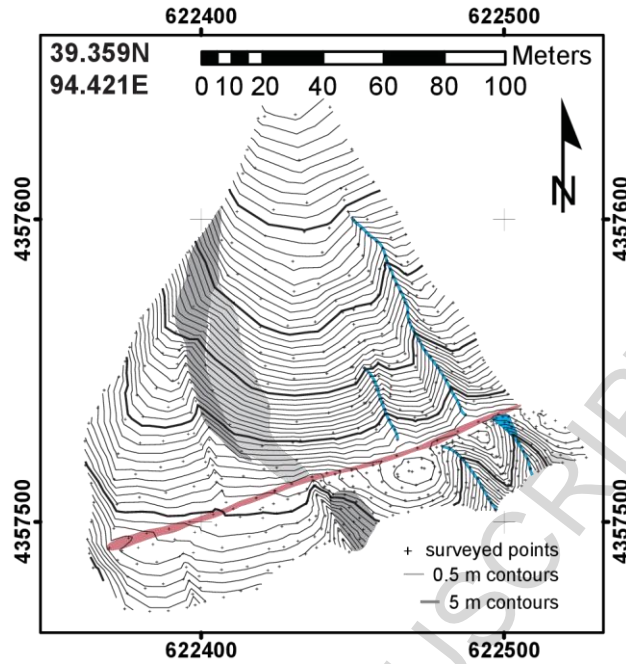


Figure 9: SATF Dangjin Shankou Total Station survey. Fault and stream thalwegs annotated; terrace riser indicated by shading. Compare to map in Figure 7.

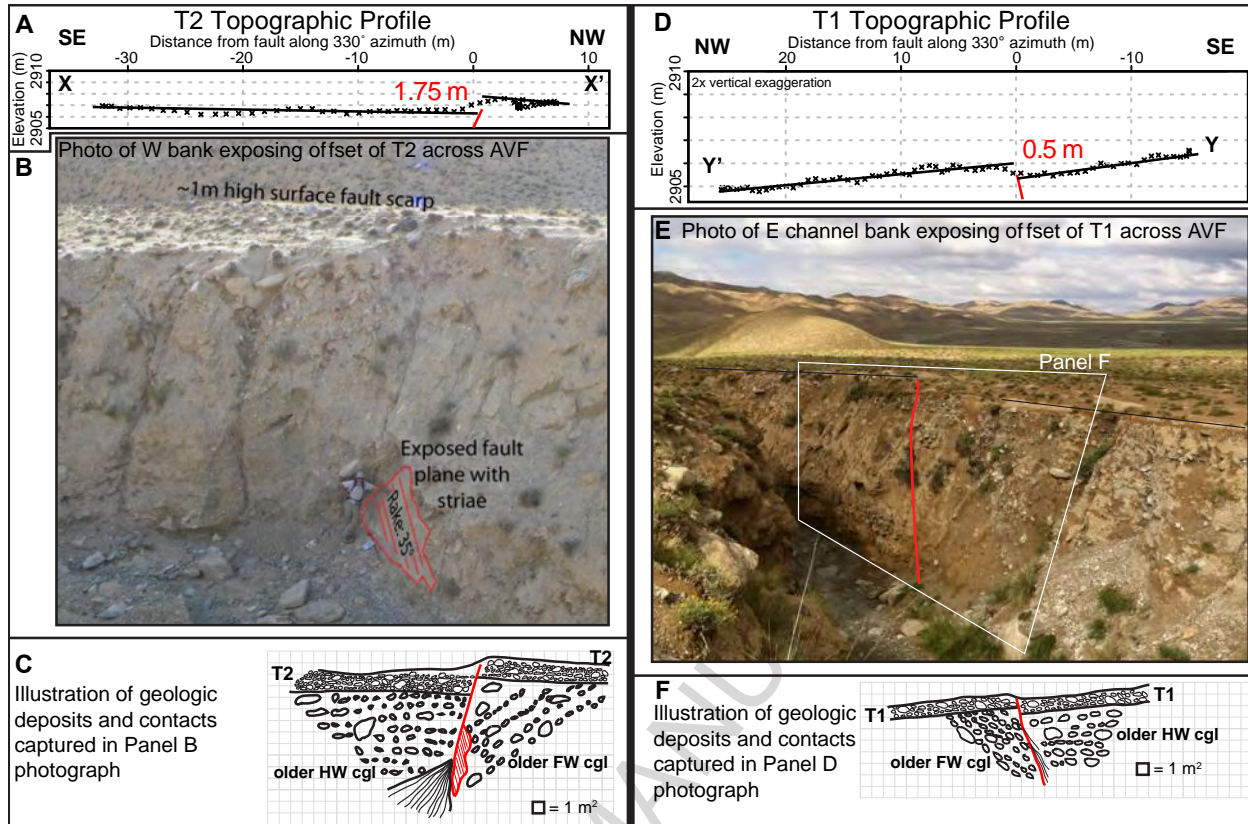


Figure 10: Annotated cross-section exposures and topographic surveys of offset fan deposits across Annanba Valley Fault. A) & D) dGPS transects downstream atop T2 & T1 surface margins, respectively, projected onto profile line oriented perpendicular to strike of the fault, showing measured offsets. B) & E) field photos looking across stream at respective terraces, showing fault scarps and offsets of lag deposits. Note fault plane exposure in central gully in (B) & Hanging wall basin of Annanba Valley fault in background of (E). C) & F) sketches of exposures in photos.

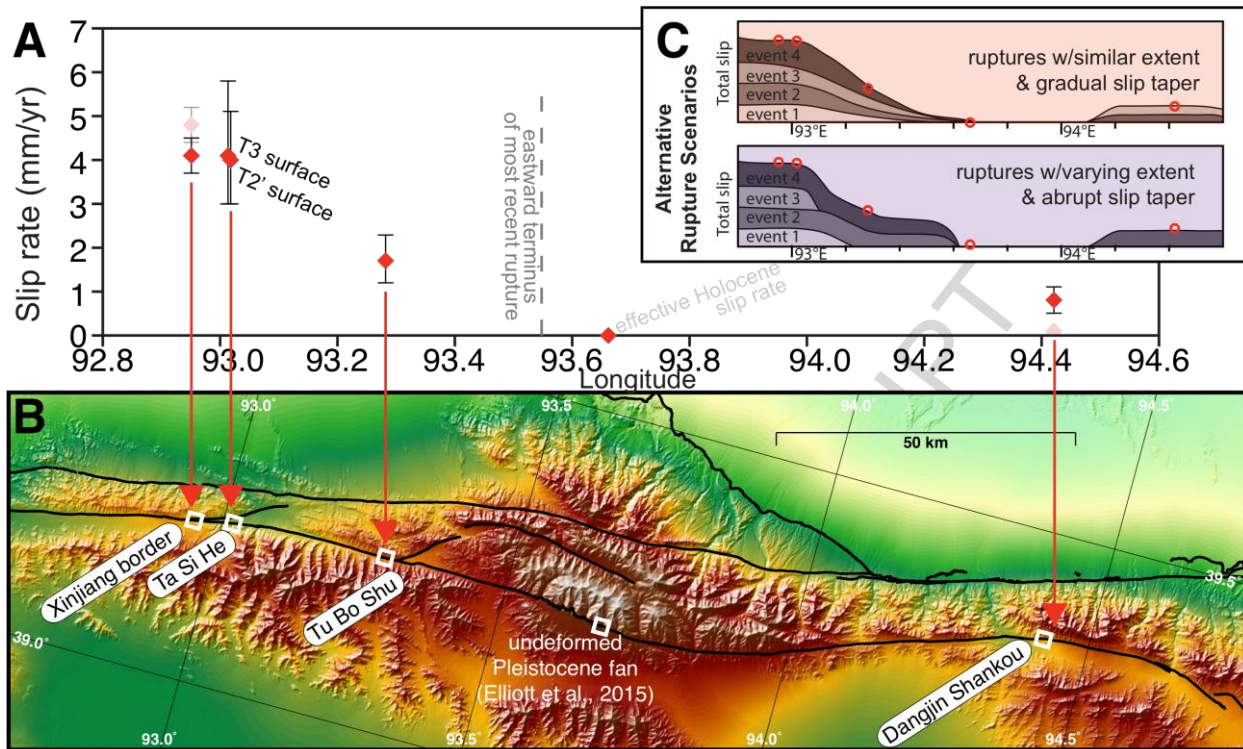


Figure 11: Plot of slip rates on the SATF around the Aksay restraining double-bend. The terminus of the MRE is plotted for reference. The Holocene slip rate declines from ~4 to 0 over 50 km between 93.0°E and 93.65°E, and does not recover in the east, where the NATF continues as the active strand. Two hypotheses of rupture recurrence that may lead to this cumulative slip distribution are illustrated. The geodetic rate across the entire fault system here is 8–10 mm/yr, so it appears at least half of the slip may be accommodated on the northern strand. Inset Panel C shows two plausible scenarios of rupture behavior that could lead to the observed slip rate gradient; each implies a different number and size of earthquakes. Compare to Fig. 1.

Feature	Sample	Depth ^a (cm)	Height ^b (cm)	Equiv. Dose ^c (Gy)	±	Dose Rate ^d (Gy/yr)	±	Age (ka)	±
SATF Xinjiang Border									
Q3 reworked loess	SATF12-L17	75.0	5.0	49.9	2.7	2.6	0.1	19.1	1.0
Q3 loess	SATF12-L19	55.0	25.0	47.3	1.4	2.9	0.1	16.4	0.5
SATF Ta Si He									
T3	SATF11-L05	50	0	25.1	5.2	3.2	0.1	7.8	1.6
T2'	SATF11-L06	40	0	15.3	0.7	3.3	0.1	4.7	0.2
SATF TuBoShu									
T2 Apex	SATF12-L20	130.0	5.0	36.6	2.0	3.4	0.1	10.8	0.6
SATF Dangjin Shankou									
T2	SATF-26L31	150	0	200.9	23.0	2.7	0.1	75.2	8.4
T2	SATF-26L32	100	50	32.6	3	3.4	0.2	9.4	1.2
T1	SATF-26L21	35	35	22.8	3	3.3	0.2	6.9	0.4
T1	SATF-26L22	70	0	31.8	2.3	3.0	0.1	10.7	0.8
Annanba Valley Fault									
T1	SATF11-L07	50	0	10.94	1.55	2.96	0.1	3.7	0.5

^a Depth below modern-day ground surface

^b Height above loess-gravel contact (top of abandoned alluvial/fluvial deposit)

^c Samples processed and analyzed using the multiple aliquot regenerative dose method in the luminescence lab of Chen Jie, IGCEA.

^d Dose rates calculated from U, K, and Th gamma ray spectrometry measurements following energy conversions of *Adamiec and Aitken* (1998).

Table 1: Optically Stimulated Luminescence burial-age measurements from basal loess samples on offset, abandoned alluvial surfaces.

Sample ID	Depth ^a (cm)	Height ^b (cm)	Analytical Results ^c						OxCal results (cal. Years BP) ^e				
			frac. Modern ^d	±	D14C (%)	±	14C age (BP)	±	max	min	median	mean	±
Ta Si He T3													
SATF11-C02	16	33	0.7792	0.0031	-220.766	3.059	2005	35	2048	1876	1955	1956	44
SATF11-C11	22	28	0.8123	0.0011	-187.727	1.115	1670	15	1614	1530	1564	1570	27
Ta Si He T2'													
SATF11-C06	20	30	0.7327	0.0010	-267.259	0.985	2500	15	2717	2493	2575	2589	65
SATF11-C07	40	25	0.7345	0.0011	-265.470	1.059	2480	15	2709	2470	2581	2585	72
SATF11-C10	23	22	0.7891	0.0115	-210.947	11.527	1900	120	2134	1552	1842	1845	149
SATF11-C12	44	14	0.7160	0.0027	-284.000	2.696	2685	35	2851	2749	2788	2796	31
SATF11-C13	45	15	0.7147	0.0030	-285.281	3.022	2700	35	2861	2752	2802	2805	32
SATF11-C15	38	23	0.7353	0.0013	-264.666	1.299	2470	15	2708	2370	2592	2580	82
Dangjin Shankou T1													
SATF-26C01	40	30	0.4554	0.0169	-544.639	16.940	6320	300	7784	6505		7175	310

^a Depth below modern-day ground surface

^b Height above loess-gravel contact (top of abandoned alluvial/fluvial deposit)

^c Samples were prepared, processed, and analysed at the KeckCAMS facility, UC Irvine

^d Radiocarbon concentrations given as fractions of the Modern standard, D¹⁴C, & conventional radiocarbon age, following conventions of Stuiver & Polach (Radiocarbon, v. 19, p.355, 1977).

^e Ages were calibrated using InterCal13 (Reimer et al., 2013) with the calibration software OxCal version 4.2.3 (Bronk & Ramsey 2013).

Table 2: Radiocarbon measurements of charcoal pieces collected from capping loess deposits on abandoned surfaces

Feature	Sample ID	Quartz mass (g)	Measured ¹⁰ Be (x10 ⁶ atoms/g Qtz)	error	Apparent Age (ka)	Corrected Age (ka)	Error (ka)
modern wash	SATF09-BC0	30.110	0.18	0.014	4.9	0	0.4
T3	SATF09-BC1	30.976	0.73	0.014	19.6	14.1	0.5
T2'	SATF09-BC2	29.262	0.34	0.013	9.2	4.2	1.7
T1	SATF09-BC3	29.414	0.37	0.011	10.0	5.0	0.8

Table 3: Be-10 amalgamated boulder-top sample measurements from Ta Si He. Samples processed in the cosmogenic radionuclide lab at Stanford University and analyzed by the PRIME lab at Purdue University.

Site	Longitude	Feature	Offset (m)	±	Age (ka)	±	Slip Rate	±
Xinjiang	92.951	Q4 incised channels	79	3	19.1	1.0	4.1	0.4
Ta Si He	93.018	T3 surface	32	4	7.8	1.6	4.1	1.7
		T2' surface	19	4	4.7	0.2	4.0	1.1
Tuboshu	93.282	T2 fan apex	19	5	10.8	0.6	1.8	0.6
Dangjin Shankou	94.421	T2 incised channels	9	2	10.7	0.8	0.8	0.3

Table 4: Ages, Offsets, and Slip Rates at the Aksay bend

ACCEPTED MANUSCRIPT

References

- Adamiec, G., and M. Aitken (1998), Dose-rate conversion factors: update, *Ancient TL*, 16(2), 37–50.
- Avouac, J.-P. (2015), From Geodetic Imaging of Seismic and Aseismic Fault Slip to Dynamic Modeling of the Seismic Cycle, *Annual Review of Earth and Planetary Sciences*, 43(1), 150223150959,000, 10.1146/annurev-earth-060614-105302.
- Avouac, J.-P., and P. Tapponnier (1993), Kinematic Model of Active Deformation in Central Asia, *Geophysical Research Letters*, 20(10), 895–898.
- Baljinnyam, I., et al. (1993), Ruptures of Major Earthquakes and Active Deformation in Mongolia and its Surroundings, *Geological Society of America Memoir, Special Pub. 181*, 62pp.
- Barnhart, W. D., R. W. Briggs, N. G. Reitman, R. D. Gold, and G. P. Hayes (2015), Evidence for slip partitioning and bimodal slip behavior on a single fault: Surface slip characteristics of the 2013 Mw7.7 Balochistan, Pakistan earthquake, *Earth and Planetary Science Letters*, 420, 1–11, 10.1016/j.epsl.2015.03.027.
- Bendick, R., R. G. Bilham, J. T. Freymueller, K. Larson, and G. H. Yin (2000), Geodetic evidence for a low slip rate in the Altyn Tagh fault system, *Nature*, 404(6773), 69–72, 10.1038/35003555.
- Biasi, G. P., and Weldon, R. J. I. (2006), Estimating surface rupture length and magnitude of paleoearthquakes from point measurements of rupture displacement. *Bulletin of the Seismological Society of America*, 96(5), 1612–1623. <https://doi.org/10.1785/0120040172>.
- Blisniuk, K., T. K. Rockwell, L. A. Owen, M. E. Oskin, C. Lippincott, M. W. Caffee, and J. Dortch (2010), Late Quaternary slip rate gradient defined using high-resolution topography and ¹⁰Be dating of offset landforms on the southern San Jacinto Fault zone, California, *Journal of Geophysical Research*, 115(B8), B08,401, 10.1029/2009JB006346.
- Chen, Y., S.-H. H. Li, and B. Li (2012), Slip rate of the Aksay segment of Altyn Tagh Fault revealed by OSL dating of river terraces, *Quaternary Geochronology*, 10, 291–299, 10.1016/j.quageo.2012.04.012.
- Chen, Y., S.-H. H. Li, J. Sun, and B. Fu (2013), OSL dating of offset streams across the Altyn Tagh Fault: Channel deflection, loess deposition and implication for the slip rate, *Tectonophysics*, 594, 182–194, 10.1016/j.tecto.2013.04.002.
- Cowgill, E., A. Yin, T. M. Harrison, and X. F. Wang (2003), Reconstruction of the Altyn Tagh fault based on U-Pb geochronology: Role of back thrusts, mantle sutures, and heterogeneous crustal strength in forming the Tibetan Plateau, *Journal of Geophysical Research-Solid Earth*, 108(B7), 10.1029/2002jb002080.
- Cowgill, E., A. Yin, J. R. Arrowsmith, W. Xiao Feng, Z. Shuanhong, X. F. Wang, S. H. Zhang, and W. X. Feng (2004), The Akato Tagh bend along the Altyn Tagh fault, northwest Tibet 1: Smoothing by vertical-axis rotation and the effect of topographic stresses on bend-flanking faults, *Bulletin of the Geological Society of America*, 116(11-12), 1423–1442, 10.1130/B25359.1.
- Cowgill, E., R. D. Gold, X. Chen, X. F. Wang, J. R. Arrowsmith, and J. Southon (2009), Low Quaternary slip rate reconciles geodetic and geologic rates along the Altyn Tagh fault, northwestern Tibet, *Geology*, 37(7), 647–650, 10.1130/G25623a.1.
- Dawers, N. H., and Anders, M. H. (1995), Displacement-Length Scaling and Fault Linkage. *Journal of Structural Geology*, 17(5).
- Delville, N., N. Arnaud, U. M. R. Cnrs, U. B. Pascal, F. Roger, M. Brunel, P. Tapponnier, E. R. Sobel, and J.-M. Montel (2001), Paleozoic to Cenozoic deformation along the Altyn Tagh fault in the Altun Shan massif area, eastern Qilian Shan, northeastern Tibet, China, *Geological Society of America Memoir*, 194(Paleozoic and Mesozoic tectonic evolution of central Asia: from continental assembly to intracontinental deformation), 269–292.
- Duan, B., and D. D. Oglesby (2005), Multicycle dynamics of nonplanar strike-slip faults, *Journal of Geophysical Research-Solid Earth*, 110(B3), 10.1029/2004JB003298.
- Duan, B., and D. D. Oglesby (2006), Heterogeneous fault stresses from previous earthquakes and the effect on dynamics of parallel strike-slip faults, *Journal of Geophysical Research-Solid Earth*, 111(B5), doi 10.1029/2005jb004138.

- Elliott, A. J., M. E. Oskin, J. Liu-Zeng, and Y. Shao (2015), Rupture termination at restraining bends: The last great earthquake on the Altyn Tagh Fault, *Geophysical Research Letters*, 42(7), 2164–2170, 10.1002/2015GL063107.
- England, P. C., and P. Molnar (1997 a), Active deformation of Asia: From kinematics to dynamics, *Science*, 278(5338), 647–650.
- England, P. C., and P. Molnar (1997 b), The field of crustal velocity in Asia calculated from Quaternary rates of slip on faults, *Geophysical Journal International*, 130(3), 551–582.
- England, P. C., and P. Molnar (2005), Late Quaternary to decadal velocity fields in Asia, *Journal of Geophysical Research-Solid Earth*, 110(B12), 10.1029/2004jb003541.
- Gan, W., P. Zhang, Z.-K. Shen, Z. Niu, M. Wang, Y. Wan, D. Zhou, and J. Cheng (2007), Present-day crustal motion within the Tibetan Plateau inferred from GPS measurements, *Journal of Geophysical Research*, 112(B8), B08,416, 10.1029/2005JB004120.
- Gao M., Xu X., Klinger Y., Van der Woerd J., Tapponnier P., (2017), High-resolution mapping based on an unmanned aerial vehicle (UAV) to capture paleoseismic offsets along the Altyn-Tagh fault, China, *Scientific Reports*, 7(8281), doi : 10.1038/s41598-017-08119-2.
- Gold, R. D., E. Cowgill, J. R. Arrowsmith, J. C. Gosse, X. Chen, X. F. X.-f. Wang, and J. Ramo (2009), Riser diachroneity, lateral erosion, and uncertainty in rates of strike-slip faulting: A case study from Tuzidun along the Altyn Tagh Fault, NW China, *Journal of Geophysical Research-Solid Earth*, 114(B4), 1–24, 10.1029/2008JB005913.
- Gold, R. D., E. Cowgill, J. R. Arrowsmith, X. Chen, W. D. Sharp, K. M. Cooper, and X.-F. X.-f. Wang (2011), Faulted terrace risers place new constraints on the late Quaternary slip rate for the central Altyn Tagh fault, northwest Tibet, *Geological Society of America Bulletin*, 123(5/6), 958–978, 10.1130/B30207.1.
- Hamling, I. J., S. Hreinsdóttir, K. Clark, J. Elliott, C. Liang, E. Fielding, N. Litchfield, P. Villamor, L. Wallace, T. J. Wright, E. D’Anastasio, S. Bannister, D. Burbidge, P. Denys, P. Gentle, J. Howarth, C. Mueller, N. Palmer, C. Pearson, W. Power, P. Barnes, D. J. A. Barrell, R. Van Dissen, R. Langridge, T. Little, A. Nicol, J. Pettinga, J. Rowland, and M. Stirling (2017), Complex multifault rupture during the 2016 Mw 7.8 Kaikōura earthquake, New Zealand, *Science*, 7194(April), eaam7194, 10.1126/science.aam7194.
- Harris, R. A., and S. M. Day (1993), Dynamics of Fault Interaction - Parallel Strike-Slip Faults, *Journal of Geophysical Research-Solid Earth*, 98(B3), 4461–4472.
- Hollingsworth, J., L. Ye, and J.-P. Avouac (2017), Dynamically triggered slip on a splay fault in the Mw 7.8, 2016 Kaikōura (New Zealand) earthquake, *Geophysical Research Letters*, 44(Figure 1), 1–9, 10.1002/2016GL072228.
- Houseman, G. A., and P. C. England (1993), Crustal Thickening Versus Lateral Expulsion in the Indian-Asian Continental Collision, *Journal of Geophysical Research*, 98(93), 12,233–12,249, 10.1029/93JB00443.
- Jolivet, R., R. Cattin, N. Chamotrooke, C. Lasserre, and G. Peltzer (2008), Thin-plate modeling of interseismic deformation and asymmetry across the Altyn Tagh fault zone, *Geophysical Research Letters*, 35(2), Art. L02309 Doi 10.1029/2007gl031511.
- Kato, N., Satoh, T., Lei, X., Yamamoto, K., & Hirasawa, T. (1999), Effect of fault bend on the rupture propagation process of stick-slip. *Tectonophysics*, 310(1–4), 81–99, 10.1016/S0040-1951(99)00149-3.
- King, G. C. P., and J. Nábělek (1985), Role of Fault Bends in the Initiation and Termination of Earthquake Rupture, *Science*, 228(4702), 984–987.
- King, G. C. P., & Wesnousky, S. G. (2007), Scaling of fault parameters for continental strike-slip earthquakes. *Bulletin of the Seismological Society of America*, 97(6), 1833–1840, 10.1785/0120070048.
- Klinger, Y., X. Xu, P. Tapponnier, J. J. Van der Woerd, C. C. Lasserre, and G. C. P. King (2005), High-resolution satellite imagery mapping for the surface rupture and slip distribution of the Mw 7.8, 14 November 2001 Kokoxili earthquake, Kunlun fault, northern Tibet, China, *Bulletin of the Seismological Society of America*, 95(5), 1970–1987, 10.1785/0120040233.

- Lal, D. (1991), Cosmic ray labeling of erosion surfaces: in situ nuclide production rates and erosion models, *Earth and Planetary Science Letters*, 104(2-4), 424–439, 10.1016/0012-821X(91)90220-C.
- Lasserre, C., G. Peltzer, F. Crampé, Y. Klinger, J. Van der Woerd, and P. Tapponnier (2005), Coseismic deformation of the 2001 M-w=7.8 Kokoxili earthquake in Tibet, measured by synthetic aperture radar interferometry, *Journal of Geophysical Research-Solid Earth*, 110(B12), 10.1029/2004jb003500.
- Lehmkuhl, F., M. Klinge, J. Rees-Jones, and E. J. Rhodes (2000), Late Quaternary aeolian sedimentation in central and south-eastern Tibet, *Quaternary International*, 71.
- Li, H., Pan, J., Lin, A., Sun, Z., Liu, D., Zhang, J., Li, C., Liu, K., Chevalier, M.-L., Yun, K., Gong, Z. (2016). Coseismic surface ruptures associated with the 2014 MW 6.9 Yutian earthquake on the Altyn Tagh Fault, Tibetan Plateau. *Bulletin of the Seismological Society of America*, 106(2), 595–608. <https://doi.org/10.1785/0120150136>.
- Lozos, J. C., D. D. Oglesby, B. Duan, and S. G. Wesnousky (2011), The Effects of Double Fault Bends on Rupture Propagation: A Geometrical Parameter Study, *Bulletin of the Seismological Society of America*, 101(1), 385–398, 10.1785/0120100029.
- Lu, Y., X. Wang, and a.G. Wintle (2007), A new OSL chronology for dust accumulation in the last 130,000 yr for the Chinese Loess Plateau, *Quaternary Research*, 67(1), 152–160, 10.1016/j.yqres.2006.08.003.
- Mériaux, A.-S. S., P. Tapponnier, F. J. Ryerson, X. Xu, G. C. P. King, J. Van der Woerd, R. C. Finkel, H. Li, M. W. Caffee, Z. Q. Xu, W. Chen, and L. Haibing (2005), The Aksay segment of the northern Altyn Tagh fault: Tectonic geomorphology, landscape evolution, and Holocene slip rate, *Journal of Geophysical Research*, 110(B4), 1–32, 10.1029/2004JB003210.
- Molnar, P., and P. Tapponnier (1975), Cenozoic Tectonics of Asia - Effects of a Continental Collision, *Science*, 189(4201), 419–426.
- Molnar, P., B. C. Burchfiel, L. K'uangyi, and Z. Ziyun (1987), Geomorphic evidence for active faulting in the Altyn Tagh and northern Tibet and qualitative estimates of its contribution to the convergence of India and Eurasia, *Geology*, 15(3), 249–253, 10.1130/0091-7613(1987)15<249.
- Oglesby, D. D. (2008), Rupture termination and jump on parallel offset faults. *Bulletin of the Seismological Society of America*, 98(1), 440–447. <https://doi.org/10.1785/0120070163>.
- Owen, L. A., R. C. Finkel, M. Haizhou, and P. Barnard (2006), Late Quaternary landscape evolution in the Kunlun Mountains and Qaidam Basin, Northern Tibet: A framework for examining the links between glaciation, lake level changes and alluvial fan formation, *Quaternary International*, 154-155, 73–86, 10.1016/j.quaint.2006.02.008.
- Pan, B. T., D. W. Burbank, Y. X. Wang, G. J. Wu, J. J. Li, and Q. Y. Guan (2003), A 900 ky record of strath terrace formation during glacial-interglacial transitions in northwest China, *Geology*, 31(11), 957–960.
- Peltzer, G., P. Tapponnier, and R. Armijo (1989), Magnitude of Late Quaternary left-lateral displacements along the north edge of Tibet., *Science*, 246(4935), 1285–1289, 10.1126/science.246.4935.1285.
- Porter, S. C., and Z. An (2005), Episodic gullying and paleomonsoon cycles on the Chinese Loess Plateau, *Quaternary Research*, 64(2), 234–241, 10.1016/j.yqres.2005.06.010.
- Rhodes, E. J. (2011), Optically Stimulated Luminescence Dating of Sediments over the Past 200,000 Years, *Annual Review of Earth and Planetary Sciences*, 39(1), 461–488, 10.1146/annurev-earth-040610-133425.
- Ritts, B. D., and U. Biffi (2000), Magnitude of post-Middle Jurassic (Bajocian) displacement on the central Altyn Tagh fault system, northwest China, *Geological Society of America Bulletin*, 112(1), 61–74.
- Rodgers, D. W., and T. a. Little (2006), World's largest coseismic strike-slip offset: The 1855 rupture of the Wairarapa Fault, New Zealand, and implications for displacement/length scaling of continental earthquakes, *Journal of Geophysical Research*, 111(B12), B12,408, 10.1029/2005JB004065.
- Scholz, C. H., Dawers, N. H., Yu, J. Z., and Anders, M. H. (1993), Fault Growth and Fault Scaling Laws - Preliminary-Results. *Journal of Geophysical Research-Solid Earth*, 98(B12), 21951–21961.
- Schwartz, D. P., Haeussler, P. J., Seitz, G. G., & Dawson, T. E. (2012), Why the 2002 Denali fault rupture

- propagated onto the Totschunda fault: Implications for fault branching and seismic hazards. *Journal of Geophysical Research*, 117(B11), B11304, 10.1029/2011JB008918.
- Shao, Y., J. Liu-Zeng, M. E. Oskin, A. J. Elliott, and P. Wang (in review), Paleoseismic Investigation of the Aksay Restraining Double-bend, Altyn Tagh Fault, and its Implication for Barrier-breaching Ruptures, *Journal of Geophysical Research: Solid Earth*.
- Stone, J. O. H. (2000), Air pressure and cosmogenic isotope production, *Journal of Geophysical Research*, 105(1), 753–759.
- Sun, J. (2002 a), Source Regions and Formation of the Loess Sediments on the High Mountain Regions of Northwestern China, *Quaternary Research*, 58(3), 341–351, 10.1006/qres.2002.2381.
- Sun, J. (2002 b), Provenance of loess material and formation of loess deposits on the Chinese Loess Plateau, *Earth and Planetary Science Letters*, 203, 845–859.
- Sun, J., S.-H. H. Li, D. R. Muhs, and B. Li (2007), Loess sedimentation in Tibet: provenance, processes, and link with Quaternary glaciations, *Quaternary Science Reviews*, 26(17-18), 2265–2280, 10.1016/j.quascirev.2007.05.003.
- Tapponnier, P., and P. Molnar (1977), Active faulting and tectonics in China, *Journal of Geophysical Research*, 82(20), 2905–2930, 10.1029/JB082i020p02905.
- Tapponnier, P., B. Meyer, J.-P. Avouac, G. Peltzer, Y. Gaudemer, S. M. Guo, H. F. Xiang, K. L. Yin, Z. T. Chen, S. H. Cai, and H. G. Dai (1990), Active Thrusting and Folding in the Qilian-Shan, and Decoupling between Upper Crust and Mantle in Northeastern Tibet, *Earth and Planetary Science Letters*, 97(3-4).
- Tapponnier, P., F. J. Ryerson, J. Van der Woerd, A.-S. Mériaux, and C. Lasserre (2001), Long-term slip rates and characteristic slip: keys to active fault behaviour and earthquake hazard, *Comptes Rendus De L Academie Des Sciences Serie Ii Fascicule a-Sciences De La Terre Et Des Planetes*, 333(9), 483–494, 10.1016/S1251-8050(01)01668-8.
- Thatcher, W. R. (2007), Microplate model for the present-day deformation of Tibet, *Journal of Geophysical Research-Solid Earth*, 112(B1), 1–13, 10.1029/2005JB004244.
- Wang, F., X. Xu, R. Zheng, W. Chen, and P. Tapponnier (2002), Segmentation of surface ruptures on the eastern segment of the Altyn Tagh fault zone, *Seismology and Geology*, 24(2), 145–158.
- Wang, F., X. Xu, and R. Zheng (2004), Study on Holocene strike-slip rates of the middle Altyn Tagh fault by terraces offset measurement, *Seismology and Geology*, 26(1), 61–70.
- Washburn, Z., and J. R. Arrowsmith (2003), Paleoseismology of the Xorxol segment of the central Altyn Tagh fault, Xinjiang, China, *Annals of Geophysics*, 46(5).
- Washburn, Z., J. R. Arrowsmith, S. L. Forman, E. Cowgill, X. F. Wang, Y. Q. Zhang, Z. L. Chen, W. Xiaofeng, Z. Yueqiao, and C. Zhengle (2001), Late Holocene earthquake history of the central Altyn Tagh fault, China, *Geology*, 29(11), 1051–1054, 10.1130/0091-7613.
- Wells, D., and K. J. Coppersmith (1994), New empirical relationships among magnitude, rupture length, rupture width, rupture area, and surface displacement, *Bulletin of the Seismological Society of America*, 84(4), 974–1002.
- Wesnousky, S. G. (2006), Predicting the endpoints of earthquake ruptures, *Nature*, 444(7117), 358–360, Doi 10.1038/Nature05275.
- Woerd, J. V. D., X. Xu, L. Haibing, P. Tapponnier, B. Meyer, F. J. Ryerson, A.-S. Meriaux, X. Zhiqin, and J. Van der Woerd (2001), Rapid active thrusting along the northwestern range front of the Tanghe Nan Shan (western Gansu, China), *Journal of Geophysical Research*, 106(B12), 30,475–30,504, 10.1029/2001JB000583.
- Xu, X., P. Tapponnier, J. Van der Woerd, F. J. Ryerson, F. Wang, Z. Rongzhang, C. Wenbin, M. Wentao, Y. Guihua, C. Guihua, A.-S. A.-S. Mériaux, R. Zheng, W. Chen, W. Ma, G. Yu, G. Chen, A.-S. Meriaux, Z. Rongzhang, C. Wenbin, M. Wentao, Y. Guihua, C. Guihua, and A.-S. A.-S. Mériaux (2005), Late Quaternary sinistral slip rate along the Altyn Tagh, *Science in China Series D Earth Sciences*, 48(3), 384–397, 10.1360/02yd0436.
- Yin, A., and T. M. Harrison (2000), Geologic Evolution of the Himalayan-Tibetan Orogen, *Annual Review of Earth and Planetary Sciences*, 28(1), 211–280, 10.1146/annurev.earth.28.1.211.

- Yue, Y. J., B. D. Ritts, and S. A. Graham (2001), Initiation and long-term slip history of the Altyn Tagh fault, *International Geology Review*, 43(12), 1087–1093.
- Zhang, P., P. Molnar, and X. Xu (2007), Late Quaternary and present-day rates of slip along the Altyn Tagh Fault, northern margin of the Tibetan Plateau, *Tectonics*, 26(5), 1–24, 10.1029/2006TC002014.
- Zinke, R., J. Hollingsworth, and J. F. Dolan (2014), Surface slip and off-fault deformation patterns in the 2013 Mw 7.7 Balochistan, Pakistan earthquake: Implications for controls on the distribution of near-surface coseismic slip, *Geochemistry Geophysics Geosystems*, 15, 1–17, 10.1002/2014GC005538.

ACCEPTED MANUSCRIPT

Persistent Rupture Terminations at a Restraining Bend from Slip Rates on the eastern Altyn Tagh Fault

Elliott, et al.

Highlights

- Left-lateral slip-rate on one strand of the eastern Altyn Tagh Fault declines from ~ 4 mm/yr to < 1 mm/yr as the fault takes a large transpressional double-bend
- Correspondence of observed slip rate gradient with that predicted by numerical modelling suggests it results from multiple earthquake ruptures repeatedly terminating at the bend
- A small fraction of ruptures may propagate beyond the bend, showing that its role as a barrier is conditional